

159291
1N-76-50
159291
P07

**Final Report to NASA
on
Aerospace Devices for Magnetic Replicas
(ID# NAG-9-592)**

by

**Roy Weinstein
Institute for Beam Particle Dynamics
University of Houston
Houston, Texas 77204-5506**

(NASA-CR-192958) AEROSPACE DEVICES
FOR MAGNETIC REPLICAS Final Report
(Houston Univ.) 67 p

N93-25667

Unclas

G3/76 0159291

Abstract

Retained persistent magnetic field has been studied and improved in the superconductor $\text{YBa}_2\text{Cu}_3\text{O}_7$ (Y123). During the study, trapped magnetic field, B_t , has been increased by over a factor of 10^5 . Methods used to improve magnetic field trapping were principally: (a). the adoption of the Melt Texturing process to increase grain size; (b). the addition of excess Y to disperse deposits of Y_2BaCuO_5 (Y211) and again increase grain size; and (c). irradiation with high energy particles including 1H^+ , 3He^{++} , 4He^{++} , and fission fragments. (d) utilizing temperatures below 77 K has also been quantified as a way to increase trapped field.

In addition, in our study of B_t , we have found laws governing creep, activation, temperature dependence, creep vs. current flow, etc.

In the range $20\text{ K} \leq T \leq 65\text{ K}$, and for $B < 10$ Tesla, a simple empirical relationship was found: $B_{\text{trap}}(T_2) = B_{\text{trap}}(T_1) [(T_c - T_2)/(T_c - T_1)]^2$, where T_c is the critical temperature.

The highest experimental trapped field was $B_{\text{trap}} = 3.96$ Tesla, at 65 K. We believe this to be the highest persistent field ever produced, by any method.

A two component model of the persistent currents has been developed. This accurately reproduces the data, using as parameters only the magnitude of a constant surface current, J_s , and a constant volume current J_v . The model successfully predicts $B_t(xyz)$ for the case of maximum trapped field, for all samples observed. It has also been extended to describe the unsaturated case either zero field cooled, or field cooled.

Loss of B_{trap} with time has been studied for the critical state ($B_{t,\text{max}}$), and non critical state ($B_t < B_{t,\text{max}}$), for times from a few minutes to a few months, for unirradiated material, for irradiation by 1H^+ , 3He^{++} , 4He^{++} , high z projectiles, and neutrons, and for all materials used in the overall study.

We conclude that: (a) multi Tesla trapped fields are attained; (b) fields over 10 T are achievable; (c) creep is not a large problem; (d) application is feasible to motors, generators, magnets for particle beam optics, separators, levitating bearings, energy storage, shielding, and transportation.

PRECEDING PAGE BLANK NOT FILMED

Table of Contents

Cover Page.....	i
Abstract.....	ii
Index.....	iii
I. <u>Introduction</u>	I.1
II. <u>Magnitude of Trapped Field</u>	II.1
A. Early Work.....	II.1
B. Melt Texturing.....	II.5
C. Activation and Saturation.....	II.8
D. Increase of J_c by Proton Bombardment.....	II.8
E. Increase of d , and J_c via Excess Y.....	II.11
F. Second Proton Bombardment, and Bombardment with 3He^{++} and 4He^{++}	II.16
G. Increases in d by Chemical and Temperature Gradients.....	II.19
H. High Z irradiation.....	II.21
I. Achievements and Predictions at 77 K.....	II.23
J. Temperature Dependence.....	II.25
K. Conclusions Concerning Magnitude of B_t	II.31
III. <u>Two Component Model of J_c</u>	III.1
A. Field Plots.....	III.1
B. Current Model.....	III.1
C. Measurement of J_c	III.6
D. A New Characterization Tool for J_c	III.7
E. The Non-Critical State.....	III.7
F. Conclusions Concerning Current Model.....	III.14
IV. <u>Creep</u>	IV.1
A. Creep Law, Critical State.....	IV.1
B. Creep, Non-Critical State.....	IV.1
V. <u>Prototyping</u>	V.1
VI. <u>References</u>	VI.1
VII. <u>Glossary of Terms</u>	VII.1

I. Introduction

Superconducting (SC) materials normally expel magnetic fields. However, imperfections in the material can result in pinning forces which trap magnetic field within the SC. These trapped magnetic fields have certain unique and useful properties.

In 1973 a group at the Stanford Linear Accelerator Center (SLAC) proposed to use low critical temperature (T_c) Type I and II superconductors, in various configurations to contain rather than expel magnetic fields^[1,2,3]. The magnetic field is trapped by imperfections in the SC, so that the field is literally "pinned" at the imperfections^[1]. The imperfections occurred naturally, or were introduced, for example, by work hardening the SC. Once pinned, the trapped magnetic field, B_t , was maintained by persistent SC currents. In low T_c materials the field was permanent, within the ability of the experimenters to measure.

Experimental tests were run by the SLAC group with various dipole, quadrupole, and sextupole magnets^[1,2,3]. SC cylinders of Pb, NbTi, and Nb₃Sn were used. Fields were trapped transversely to the axis of hollow cylinders, split hollow cylinders, and solid cylinders. Dipole magnetic fields from 1.9 to 22.4 K Gauss were trapped. To the best of our knowledge, the production of a permanent magnet with a field of 22.4 T remained as a record until recently. One method used by the SLAC group for activating the SC was to insert a cylindrical tube of SC material into an existing magnetic field (see Fig. I.1), and then cool it until it became superconducting. The activating magnet was then turned off. This is a broadly used method of activation called Field Cooling (FC). In a second method, the cylinder was cooled to its superconducting state, and then the field was turned on (see Fig. I.2). This also is a broadly used method of activation called Zero Field Cooling (ZFC). In both cases, when the external field was turned off, part of the field contained within the SC cylinder was retained, or trapped.

The practical usefulness of such a technique depends upon many variables. Perhaps the leading question is, how high a field can be retained. In the SLAC work, fields as high as 22.4 k Gauss were captured by this technique on a cylindrical sample. The cylinder was made of 44 layers of Nb₃Sn foil with dimensions of 2.54 cm I.D., 3.34 cm O.D., and 7.62 cm length. The central 3.4 cm of the 7.62 cm long cylinder retained the field within 10% of the maximum field, thus exhibiting expected edge effects. The cylinder was operated at liquid helium temperature, 4.2 K. The cylinders were constructed by helically wrapping multiple layers of superconducting ribbon around a mandrel. From the field vs. thickness curves presented, and from more fundamental considerations, it is fairly clear that 25 k Gauss could have been captured in the SLAC samples. However this was the limiting field at 4.2 K.

Potentially, one of the useful properties of the pinned fields is that they reproduce the parent field. For example Rabinowitz et al. activated a cylinder of SC materials using a sextupole magnet as a parent. The result was an accurate replica of the sextupole (see Fig. I.3). Within the accuracy of field measurements (~ 5%), the original magnetic fields were reproduced well. The persistent SC current adjusts to whatever external field is present, *as long as the SC can carry the required current*. The SC current maintains the applied field almost independent of the shape of the SC materials, reproducing the activating field. This opens the possibility of reproducing precision magnetic fields via crudely constructed bulk SC replicas. We believe that with well made samples, containing a homogeneous distribution of imperfections, the field will, for practical purposes, be perfectly reproduced. However, these possibilities remain to be tested.

Another question bearing upon usefulness of the phenomenon is the duration of the effect. In very short times (e.g. 10 sec.), in the SLAC work, some field escaped. However, after this initial efflux, the field stabilized. The SLAC group observed no further decrease, within their experimental error, in a time of about 1 week, at which time they had to proceed to other

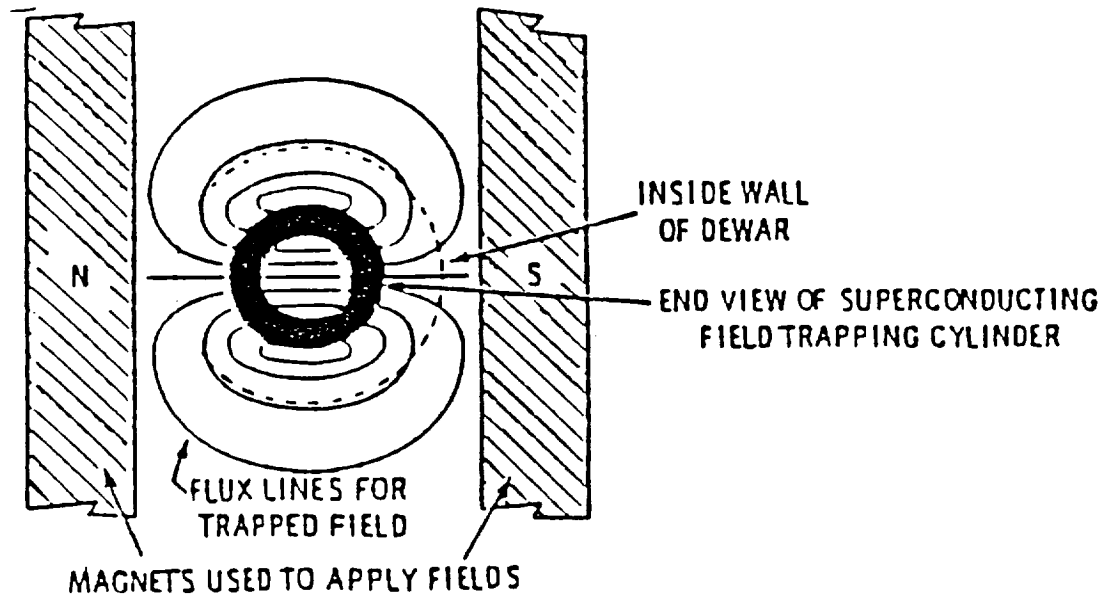


Fig. I.1 Trapped field in low temperature superconductor. Experimental arrangement used and end view schematic of the field trapped in a Nb_3Sn superconducting cylinder after the external field has been turned off.

From Ref. 3.

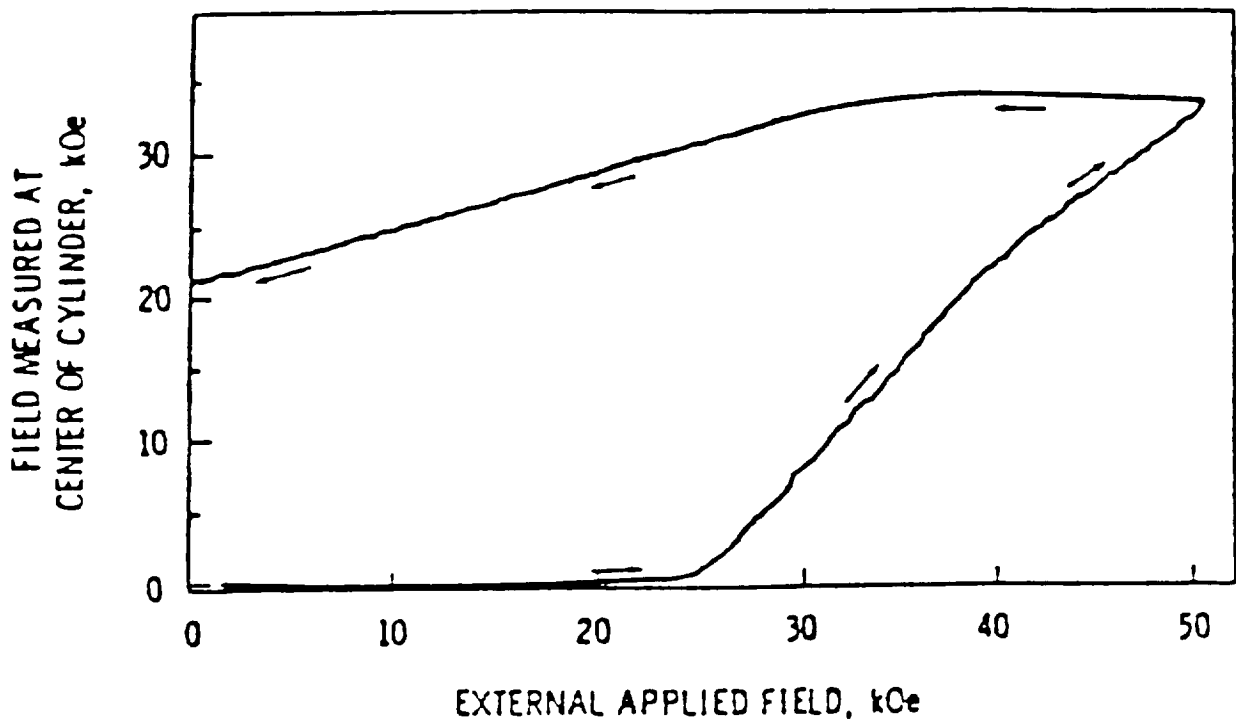


Fig. I.2 Zero field cooling, in low temperature superconductor. Trapping 21.2 kG in a 44-ribbon-layer Nb_3Sn cylinder using ZFC Activation. Field penetration and ultimately trapped field versus applied field. From Ref. 3.

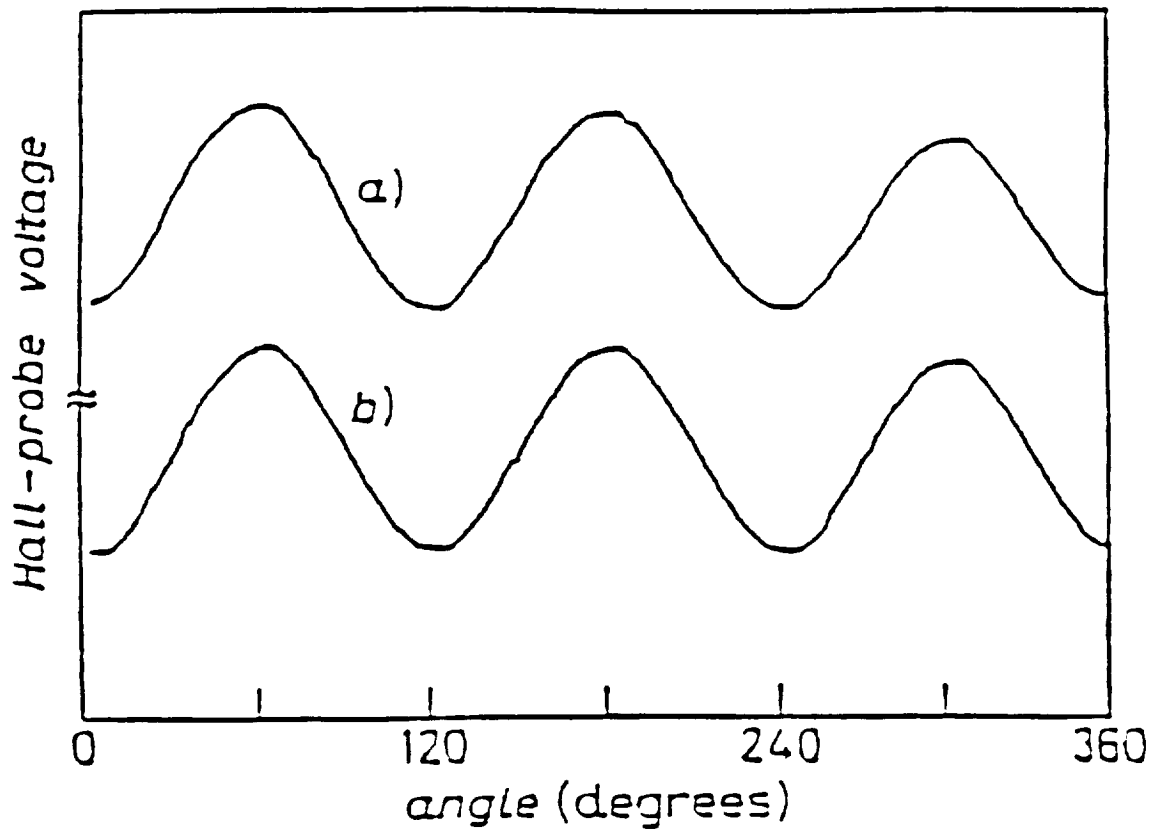


Fig. I.3 Sextupole Magnet and Replica Magnet. Radial component of magnetic field, inside Nb cylinder, vs. azimuthal angle showing a) original and b) stored sextupole field. From. Ref. 1.

work. Theoretically the life time exceeds decades, and may exceed millennia. The fields may decrease by thermally activated hopping along the pinning imperfections to the surface of the SC. This flux motion is called flux creep in analogy to the dislocation line movement in crystalline materials. For low T_c SCs, the loss due to such flux creep effect is practically zero.

The SLAC group referred to its findings as the Very Incomplete Meissner Effect (VIME).

It should be stressed that VIME devices are neither ordinary superconducting magnets nor ordinary permanent magnets, but are far simpler and fundamentally different devices. They do not need to rely heavily on geometry or dimensional tolerance. Normally, superconducting magnets rely upon precisely aligned current carrying wires or tapes to create desired field shapes. Permanent magnets also rely upon precise geometry of the magnetic materials to produce a given field. VIME devices, on the other hand, function by trapping external magnetic field, in whatever shape it may exist, and maintaining the field shape, by localized persistent SC current. They are Magnet Replicas™. Physically, the SCs behave as a permanent magnet. For example, they can be transferred to a needed location without electrical leads or connections. However, unlike wire wrapped magnets, and permanent magnets, the geometric shape and accuracy of the VIME device have little bearing on the shape and accuracy of the field. The field is copied from the parent magnet, and persistent currents adjust themselves to produce the correct field. With Magnet Replicas™, one may work toward an attractive range of industrial magnets, for use in accelerator technology, the electric power industry, aerospace, medicine, and research.

At the time of the discovery of High T_c Superconductors (HTS)^[4] we were motivated to pursue permanent magnets in these new materials. Our immediate motivation was their promise as replacements for magnets in external accelerator beam lines, which are high power consumers.

Permanent magnets made of Low Temperature Superconductors (LTS) had already exhibited significantly attractive features:

1. Energy Saving: No power is required, except for that to produce the coolant.
2. Non Critical Dimensions: The field of the replica, within the very broad limits, does not depend on the dimensions of the replica. The field shape is automatically copied from the parent magnet, which may be an accurately machined high cost device. One only needs enough superconductor to assure sufficient available current.
3. Interchangeability: A VIME magnet replica can be activated, for example, as a dipole for one period of use, and as a quadrupole for its next use. In applications involving a large number of magnets, for example in external beam lines of accelerators, this allows a reduction of inventory.

HTS permanent magnets show the *potential* for additional advantages.

4. High Fields: The extremely high upper critical field of HTS^[5] extends the theoretical limitation on the maximum achievable field to much higher values.
5. Simpler Cryostats: The higher operating temperatures of HTS make possible much simpler and cheaper cryostats. Also, the power used for cooling decreases as operating temperature increases.
6. Inexpensive Coolant: If an operating temperature of 77 K or above is chosen, liquid nitrogen can be used as a cheap and efficient coolant. It is about a factor of 200 better than liquid helium.

7. Avoidance of Wire Problem: There is a well known difficulty in producing flexible high current wire from the ceramic HTS materials. VIME devices will work even if it should prove impossible to produce wires or tapes with the new high T_c SC materials. This is because VIME devices can function based on localized *internal* persistent currents, in bulk materials. They can be made of blocks of HTS material.

8. Weight: Where weight is important, HTS permanent magnets have a significant advantage over, for example, ferro-electromagnets. The large bulk of iron and copper in principle can be avoided. The HTS material itself has a density of 6 (for $YBa_2Cu_3O_7$), compared to 7.87 for Fe and 8.96 for Cu.

Drawbacks of HTS

Although high T_c superconductors are attractive, they have well known problems. A variety of major problems are associated with the so-called weak link problem of the grain boundaries, and with the poor mechanical properties of these high T_c ceramics. The weak links result in much reduced current through grain boundaries. The ceramic properties make difficult the production of flexible wire. Although it has been demonstrated that wires or tapes can be produced with high T_c materials, the superconducting properties of these wires or tapes are very disappointing and far from practical application even after 5 years of intensive work on a world scale. As indicated above, permanent SC magnets may by-pass the wire or tape fabrication problem, at least for the production of high magnetic fields. However, the weak link problem must be solved even for such permanent magnets.

Another problem with HTS materials is that loss of field due to creep, negligible for LTS as described above, is much larger for HTS.

We have, we believe, made good progress toward taking advantage of the potential of HTS permanent magnets, and learning to eliminate or control their drawbacks. Our progress on these issues will be the subject of most of the remainder of this report.

II. Magnitude of Trapped Field

A. Early Work

An experiment on field trapping is shown schematically in Fig. II.1.

The SC sample is activated in an external field, by cooling in a cryostat. At 77 K, that cryostat can be a thin Styrofoam container. The SC sample may be cooled in a magnetic field (FC) or it may be cooled in zero field and the field then turned on (ZFC). The field is measured, typically, by a Hall probe.

Our earliest samples were constructed in the form of hollow cylinders in the manner of the work previously done^(1,2,3). The schematic of Fig. II.1 shows a hollow cylinder, with the hall probe entering axially.

Our earliest experiment was a significant disappointment, and achieved trapped field of only $B_{\text{trap}} \sim 0.3$ Gauss in a *sintered* cylinder of $\text{YBa}_2\text{Cu}_3\text{O}_{7-x}$ (Y123).

Eventually, by improving purity of materials, packing powders, adding 15% silver, and improving processing, trapped fields of 10-50 Gauss were obtained in sintered materials. Fig. II.2 shows data taken on an early cylinder which trapped 20 Gauss. The ZFC activation method was used, in which field is turned on after the sample is cooled. Note the similarity of results on HTS (Fig. II.2) and LTS materials (Fig. I.2). The flat portion of the curve of Figs. I.2 and II.2, at the outset of the cycle, is caused by the superconducting cylinder acting to shield the inner region from magnetic field. Note that in both HTS and LTS, the amount of field shielded is approximately equal to the field later trapped.

The sample used in Fig. II.2, and all early samples, were sintered. High temperature superconductor (HTS), processed by sintering, suffers the drawback of low critical-current density, J_c . J_c is in the range of 10 to 10^3 A/cm² @ 77 K, and deteriorates significantly with increase of the external magnetic field. This is due to the profusion of weak links within the samples.

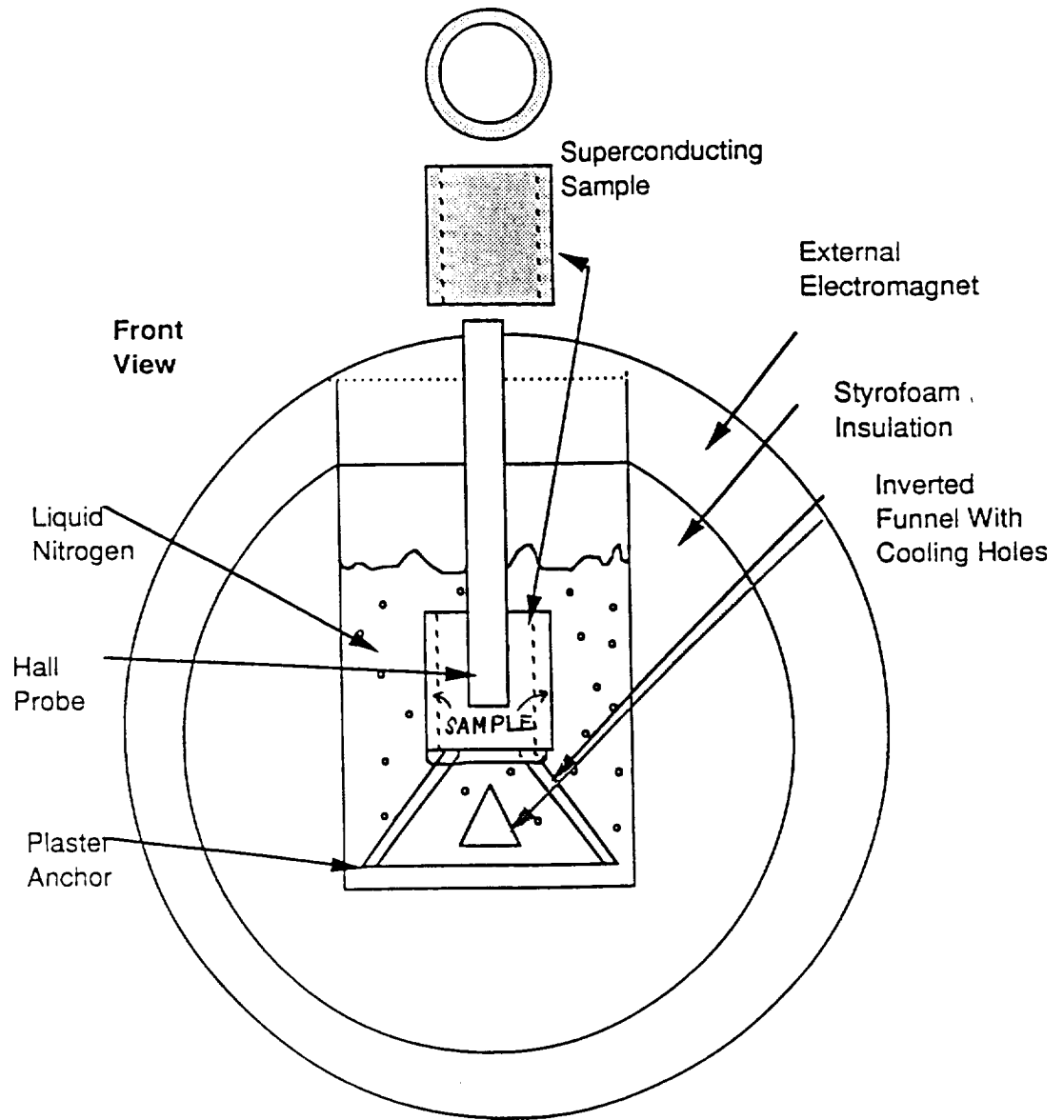
We explored 5 cylindrical samples in total, and activated samples both by FC and ZFC techniques. Our best results for sintered samples were achieved by adding circa 15% Ag, by weight. About 50 Gauss was trapped.

The fabrication of a cylinder took typically 2-3 mo, and cost typically \$2,000-\$5,000. In order to speed up the testing process, and reduce costs, we switched to tile shaped samples typically $1 \times 1 \times 0.3$ cm³. These took about 3 days to prepare, and cost about \$200. For a while we theoretically translated the tile data to expected cylindrical behavior. Finally, however, we used the tiles as the standard, and converted the early cylindrical results to tile results.

Table II.1 is a chronology of significant improvements in field trapping. The right hand column indicates the variables which resulted in increasing the trapped field. In the remainder of this section we will discuss in some detail the developments of the material or techniques used, and the trapped field, or the improved parameter achieved, as a result of the introduction of each technique. It will be seen in Table II.1 that the cumulative effects of the improvements have been to increase the trapped field by a factor of 10^5 .

As part of our analysis effort we developed a model of the currents which flow in the HTS to support the trapped fields. This current model will be discussed in Sec. III in some

Very Incomplete Meissner Effect Experiment Test Jig



11/15/88

Magnetic Field Perpendicular to the viewer

Fig. II.1 Schematic of HTS activation and measuring apparatus. Very incomplete Meissner effect experimental test set-up for high T_c samples.

Hysteresis Curve of 123+15% Ag Tube

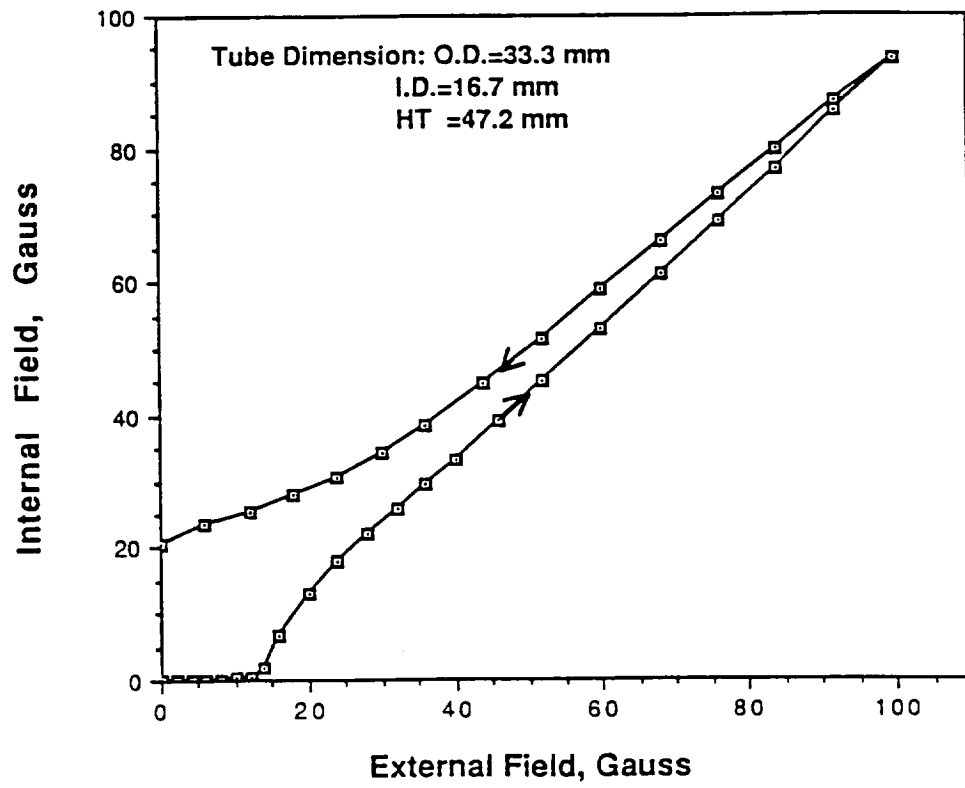


Fig. II.2 Zero field cooling experiment on high T_c sintered cylinder of Y123

Table 1 Progress in Trapped Magnetic Field in IBPD/TCSUH

Date	B _T	Comment
12/88	0.3	Poor SC, Sintered Powder
2/89	2.0	<u>Good SC</u> , Sintered Powder
4/89	4.5	Optimum <u>Thickness</u> , Sintered
5/89	10.0	<u>Ag added</u> , Sintered
6/89	80.0	<u>mm size single grain</u> , melt textured
8/89	380.0	<u>~ cm size grain</u> , no Ag, a,b Plane, melt textured
9/89	600.0	<u>Saturating "Parent" field</u> , no Ag, MT cm size grain b,c plane.
10/89	1,280.0	Same as 9/89; <u>mini-magnet</u> prototype
6/90	1,500.0	<u>Proton irradiated melt-textured</u> , single tile
7/90	4,380.0	Same as 6/90; <u>mini-magnet</u> prototype
11/90	8,587.0	Doped sample, not irradiated. <u>65K**</u> . <u>Mini-magnet</u> . B _{T,max} = 3,016G @ 77K.
4/91	1,500.0	<u>Single tile, excess Y</u> , not irradiated.
6/91	6,418.0	Same as 4/91; <u>Proton irradiated</u> , single tile, 1.4 x 1.4 x 0.4 cm ³ .
7/91	14,200.0	Same as 6/91, <u>mini-magnet</u> prototype. 5 tiles
12/91	2,200.0	Single tile, <u>chemical and T gradients</u> , not irradiated. d = 2 cm
6/92	19,000	Two tile mini-magnet, 1.2 x 1.2 x 0.6 MTY123, 1H ⁺ and 3He ⁺⁺ irradiated. Low Temperature. Limited by activation magnet.
10/92	15,250	8 tile mini-magnet, 1.2 x 1.2 x 1.5 cm ³ , light ion irradiated.
11/92	39,600	Same as 10/92, 64.5 K. Not limited by activation magnet.

*All results are at 77 K, unless otherwise stated.

detail. The model is in basic agreement with other, long standing models of persistent current, but is easier to use. We introduce here only one result of the model, in order to clarify the reasons for the diverse experimental directions, described below, which we took in our attempts to increase the trapped field, B_t . The field trapped in a round sample of diameter d and critical current J_c can be represented to a good approximation as

$$B_{\text{trap}} \propto J_c f(d) \quad \text{Eq. II.1}$$

where J_c is the critical current density in the SC, and $f(d)$ is a monotonically increasing function of d . Table II.2 presents data to provide some "feel" for $f(d)$. Details will be given in Sec. III.

Table II.2. Effect of Grain Diameter, d

An example is given with $J_s = 0$, $J_v = 30,000 \text{ A/cm}^2$, for a single tile 2 mm thick. $B_{T,\text{max}}$ is calculated at the surface of the sample.

$d(\text{cm})$	0.5	1.0	2.0	4.0	8.0
$B_{T,\text{max}}$ (Gauss)	3933	6178	8655	11,177	13,667

Following Eq. II.1, one may increase B_{trap} by increasing either J_c , or by increasing the sample diameter d . During the course of this work, B_t has been increased by a factor of 10^5 . We outline below the methods by which J_c and d have been increased in order to achieve this.

B. Melt Texturing

The problem with sintered material is that d is very small. Large currents flow in small grains. The inter grain currents are low because of "weak links," one of the difficulties with HTS materials. In sintered HTS, for example, intra grain currents of $10,000 \text{ A/cm}^2$ may flow, while inter grain currents are limited to $10 - 100 \text{ A/cm}^2$. The overall field then looks a lot like that of a ferromagnet since many small vortices create the field. Fig. II.3 shows the field of a permanent ferromagnet, and Fig. II.4 shows the field of a sintered HTS persistent magnet. The solid curves are the theory reported in Sec. III.

Following work by S. Jinn⁽⁶⁾, a processing technique called Melt Texturing (MT) was developed by the group of K. Salama at Houston⁽⁷⁾. The Salama procedure included melting the sample of $\text{YBa}_2\text{Cu}_3\text{O}_7$ (Y123), and growing a quasi-crystal from the melt. The resulting crystals are imperfect in that they contain gaps, small angle intersections of conducting planes, and deposits of Y_2BaCuO_5 (Y211). However, the process eliminates large angle intersections, boundaries of separately grown crystals, and other weak links. We refer to such relatively poor quality crystals as "grains." Our early attempts to use the MT process on Y123 resulted in a significant increase in field (see Table. II.1). The early grains then grown had $d \sim 0.1 \text{ cm}$ and trapped field of $B_t \approx 80 \text{ Gauss}$ ⁽⁸⁾.

Eventually we produced grains of $d \sim 0.5 \text{ cm}$ using Salama's prescription, and achieved $B_t \sim 380 \text{ Gauss}$ ⁽⁸⁾. HTS samples processed by methods involving partial melting followed by slow cooling, called a liquid phase process, exhibit larger grains, and significant improvement in J_c , to about 10^4 A/cm^2 at 77 K. In addition, J_c is relatively insensitive to external field.

Calculated & measured magnetic field profile of two different size SmCo magnets

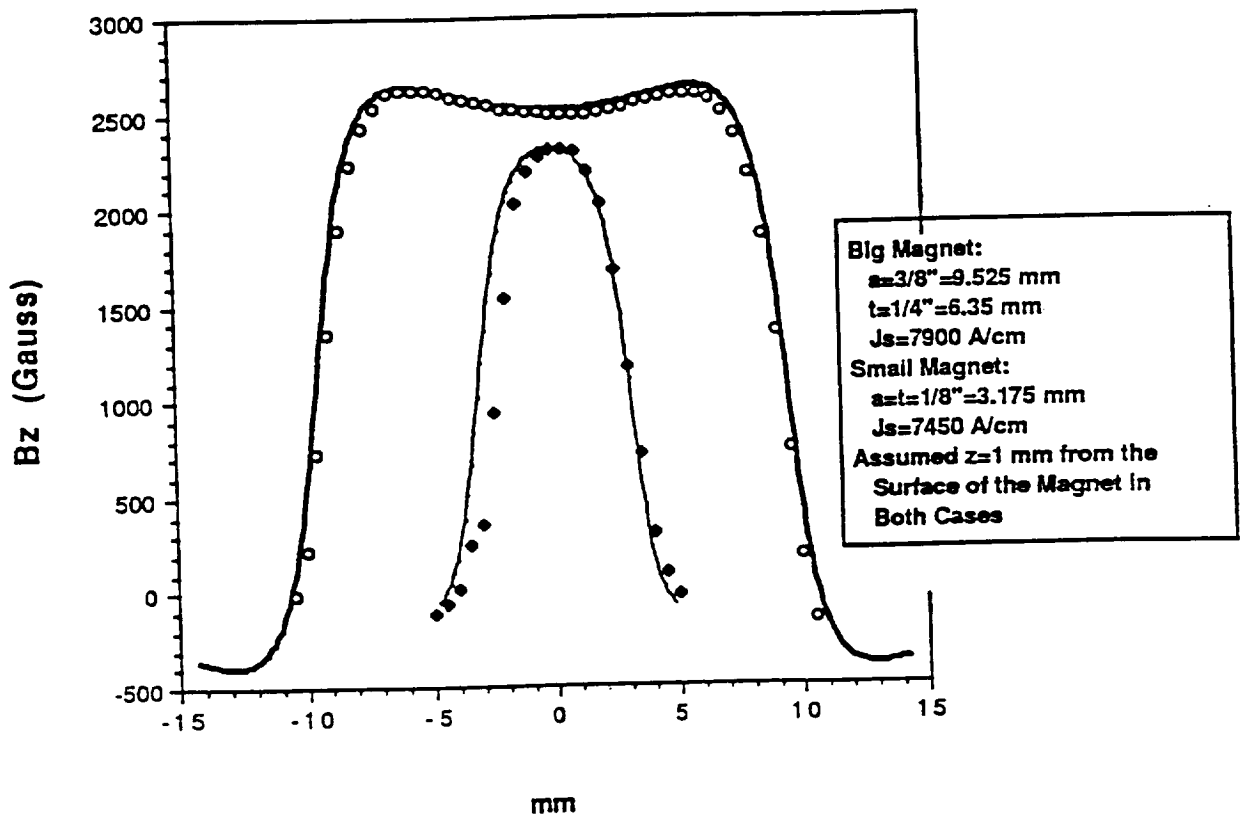


Fig. II.3 Field profile across face of permanent ferromagnet. Magnetic fields, for permanent SmCo magnets of two different aspect ratios. Solid lines are from our two component current model.

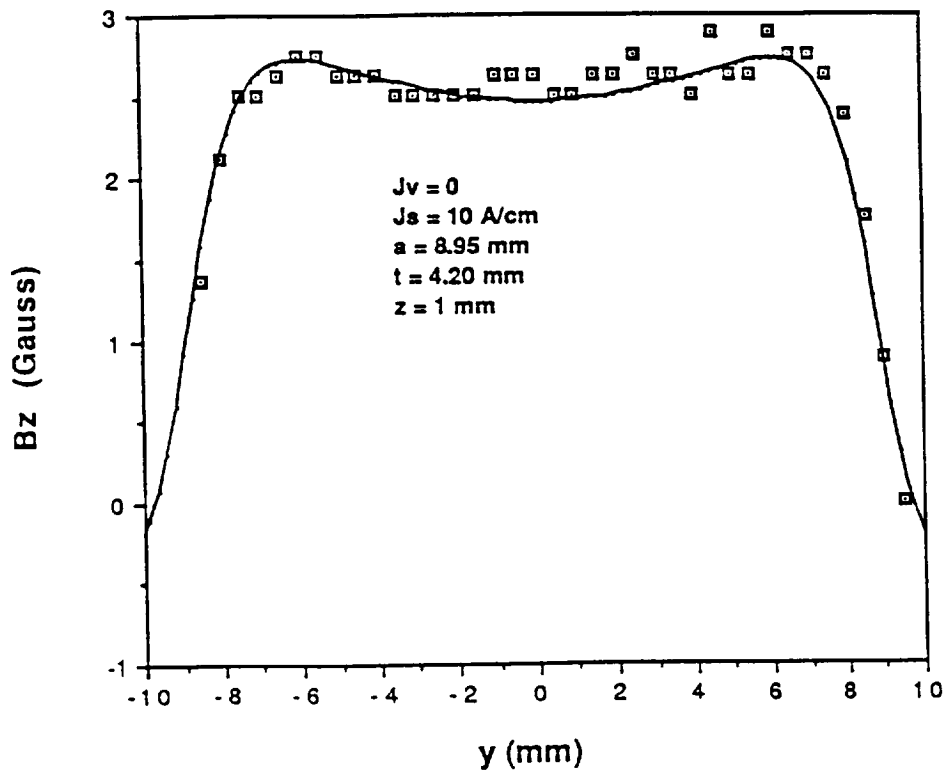


Fig. II.4 Field profile across face of sintered Y123 permanent magnet in a,b plane
Note $J_v = 0$ is required for best fit, as for permanent ferromagnet.

C. Activation and Saturation

We observed that B_t was not simply equal to the applied field, B_A . We had expected that B_t would equal B_A up to some maximum value, after which B_t could not be increased. Instead, we found that B_t behaved as

$$B_t = B_{t,\max} \left(1 - e^{-B_A/B_t}\right) \quad \text{Eq. II.2}$$

where B_t is the field trapped by FC in an applied field B_A , and $B_{t,\max}$ is the maximum trappable field⁽⁹⁾. Following this observation we tried to always measure B_t for $B_A \gg B_{t,\max}$, in order to measure a true $B_{t,\max}$. The SC in this condition is said to be *saturated*, or in the *critical state*. Fig. II.5 shows an FC activation exhibiting Eq. II.2.

D. Increase of I_c by Proton Bombardment

The first time we could afford a proton bombardment was in the Spring of 1990, although our reasons for the bombardment were stated in a patent application a year earlier. High energy particles represent a tool for uniformly inserting damage centers, which then act as flux pinning centers.

High energy protons were used for two reasons. First we were then, and are now, applications oriented. Applications require sizable magnets. High energy protons are very penetrating and can process enough material to make sizable devices. For example, a 200 MeV proton has a range of over 30 grams/cm², equal to 5 cm of Y123.

A high energy projectile of charge Z has energy losses owing to both nuclear collision and ionization loss. The later is proportional, in the non relativistic region, to Z^2/v . Initially we speculated that the ionization, because it would result in a continuous "tube" of damage, would better pin field. It turns out to be correct, as we shall see, that tubes of damage are excellent pinning centers, but we now know that the ionization of high energy protons does insufficient damage to the HTS material to accomplish this, and higher Z is needed. We did not know this at the outset, but we did intend to vary Z in order to vary ionization, to search for an optimum projectile. Section IIF will describe bombardment with higher Z projectiles.

The first proton bombardment was done at 160 MeV, using the Harvard Cyclotron. Fig. II.6 shows the envelope of the data points. The data can be approximately fit by a curve of the form

$$R \equiv \frac{B(\text{after bombard})}{B(\text{before bombard})} = 1 + (R_{\max} - 1) \left(1 - e^{-F/F_0}\right) \quad \text{Eq. II.3}$$

In Eq. II.3, F is the fluence of protons (#/cm²), and F_0 is a constant. The results of the Harvard experiment⁽¹⁰⁾ gave $R_{\max} \approx 3.7$, and $F_0 \approx 6 \times 10^{15}$.

It is expected that if bombardment fluence is increased, at some point R will decrease due to radiation damage. We have not continued to the higher values of F needed to observe a fall off in R .

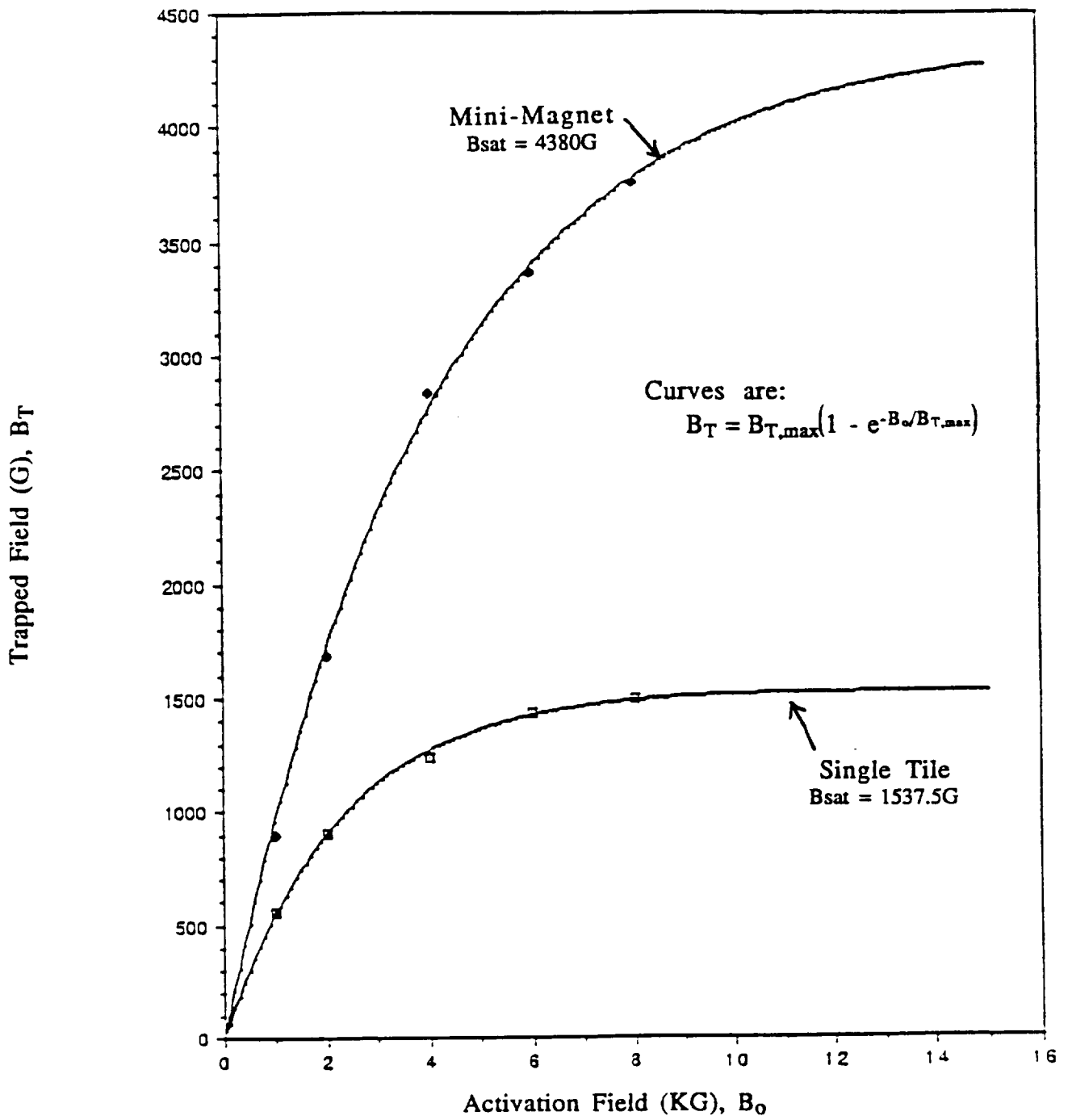


Fig. II.5 Activation curves for Y123. Fit is of form $B_T = B_{T,max}(1 - e^{-B_0/B_{T,max}})$.

Results of 160 MeV p^+ Bombardment on Melt Textured Y123

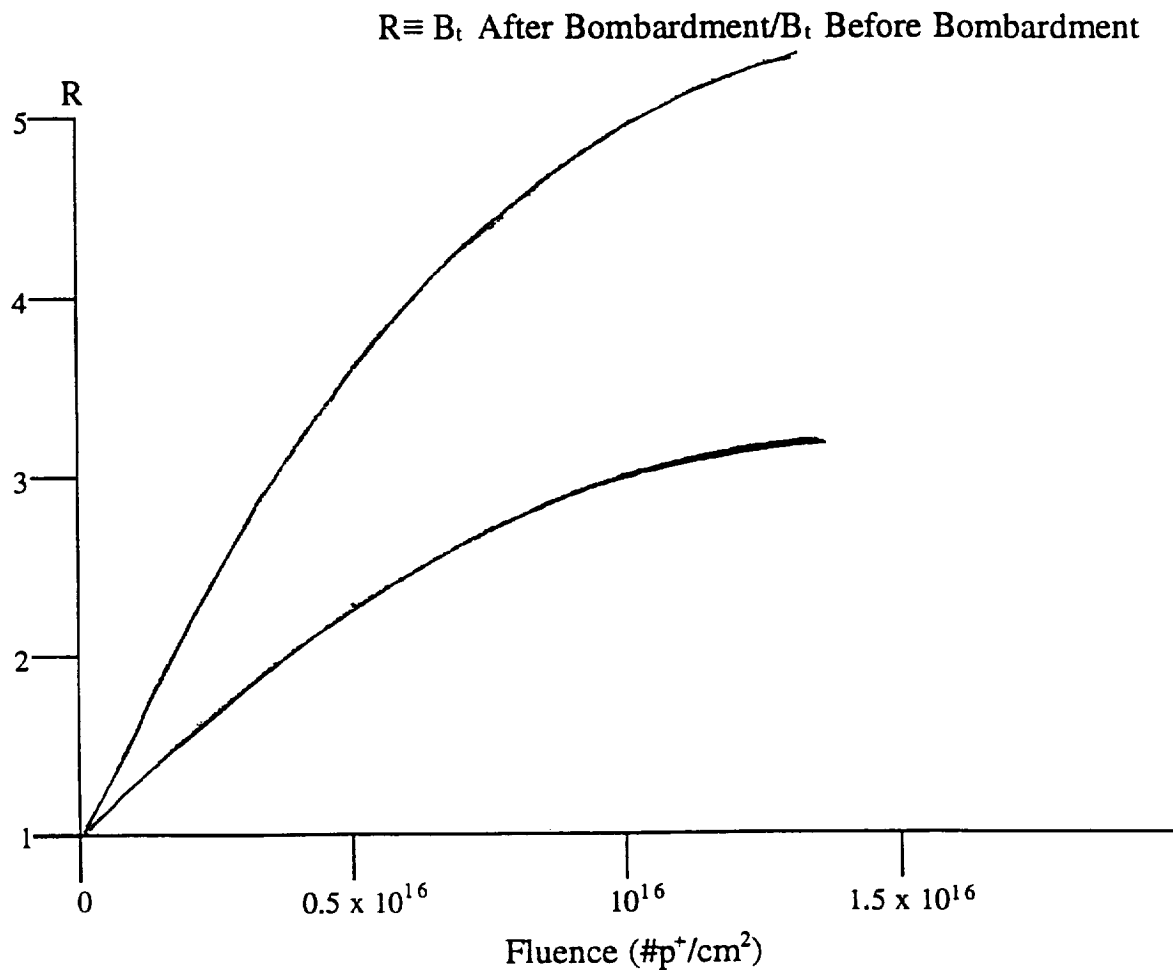


Fig. II.6 Results of proton bombardment at Harvard Cyclotron. R is defined in Eq. II.3 of the text. Curves shown are the envelopes, between which the data points lie.

The protons increase B_t by introducing pinning centers. These in turn result in higher J_c . The results of the Harvard bombardment may be restated thus: Bombardment by high energy $1H^+$, with a fluence of the order of $2 \times 10^{16}/\text{cm}^2$, increases J_c by a factor of ~ 3.7 .

Using proton irradiated, melt textured Y(123), we obtained $B_t = 1.5$ k G in a single tile and $B_t = 4.38$ k G in a mini magnet fabricated from 4 tiles. Although grain diameter was not then yet a focus of our work, we believe we were dealing with grain diameters of $d \sim 0.5$ μm .

E. Increase of d , and J_c via Excess Y

In parallel with work to introduce pinning centers by radiation (Sec. IID) we attempted to introduce chemical pinning centers. Experiments with rare earths other than Y (and Ho) had only marginal effect. However the addition of excess Y has a marked effect.

First, the grains of $\text{YBa}_2\text{Cu}_3\text{O}_7$ (Y123), or more properly $\text{Y}_{1+x}\text{Ba}_2\text{Cu}_3\text{O}_7$ (Y₁₊₂₃) which were grown with excess Y, were more uniform. Fig. II.7a shows SEM micrographs of three samples of Y123. The first has no excess Y. The second has a 20% molar excess Y, and the third has 50% molar excess Y. The production of melt textured $\text{YBa}_2\text{Cu}_3\text{O}_7$ (MT Y123) results in deposits of Y_2BaCuO_5 (Y211). Introducing larger amounts of Y has the effect of breaking up large deposits of Y211 which occur in the melt texturing process, and dispersing them. More Y211 is deposited than in stoichiometrically correct Y123, but the effect makes the Y211 deposits more uniform, and smaller. It also results in larger, more uniform single grains of Y123.

It is difficult to obtain a precise result on the effect of any one variable in melt texturing, because the other variables are difficult to control exactly. With this caveat, we note that the addition of excess Y increased grain size by about a factor of 2.

Fig. II.7a shows the results of adding the excess Y in the form of Y_2O_3 . The same qualitative result can be obtained by adding the excess Y in the form of Y_2BaCuO_5 (Y211). This is shown in the top micrographs of Fig. II.7.b. The addition of Ho_2O_3 also achieves qualitatively the same results, as shown at the bottom of Fig. II.7.b. In the collection of micrographs in Fig. II.7, the back scattered electron intensity is different for Y123 and Y211, due to the different chemical concentrations in the Y123 and Y211 phases. The Y211 phase appears to be white and the Y123 phase is darker in the figure.

Fig. II.8 shows the effect of excess Y_2O_3 on the Y211 size spectrum⁽¹¹⁾.

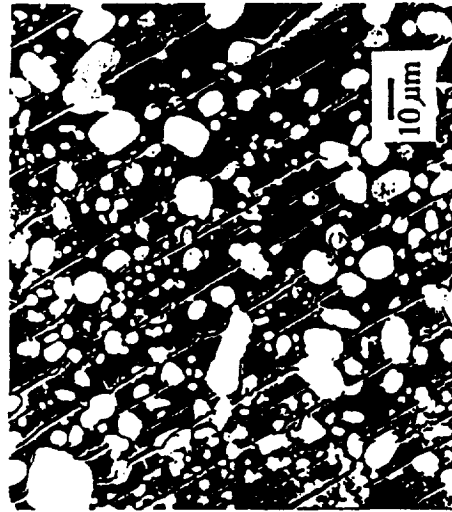
Some of the Y211 particles act as pinning centers, thereby increasing J_c , albeit by only $\leq 30\%$. It is clear from the data of others⁽¹²⁾, that the smallest Y211 particles are effective in pinning. (The pinning increases as the total *area* of Y211 in the sample⁽¹²⁾.)

The best size for pinning centers is near the coherence length (a few nm), and the Y211 particle sizes thus far achieved (μm to sub- μm) are still at least one to two orders of magnitude larger than this. The pinning is probably due to crystal deformation at the surface interface of Y211 and Y123.

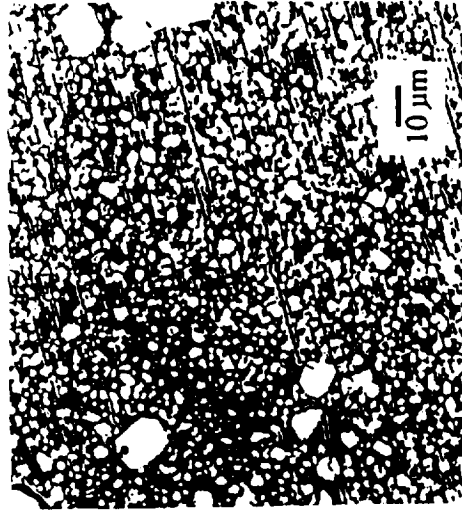
Thus, we have found that adding different amounts of Y_2O_3 or Ho_2O_3 to the $\text{YBa}_2\text{Cu}_3\text{O}_7$ mixture, and following the standard liquid phase processing⁽⁷⁾, will reduce the Y211 particle size and increase the Y123 grain size significantly. The improved grain size directly impacts B_t , via Eq. II.1. The reduced Y211 particle size marginally increases J_c .



SEM micrograph of a MT-Y123 sample without Y_2O_3 (or Ho_2O_3 and Y_2BaCuO_5) addition.



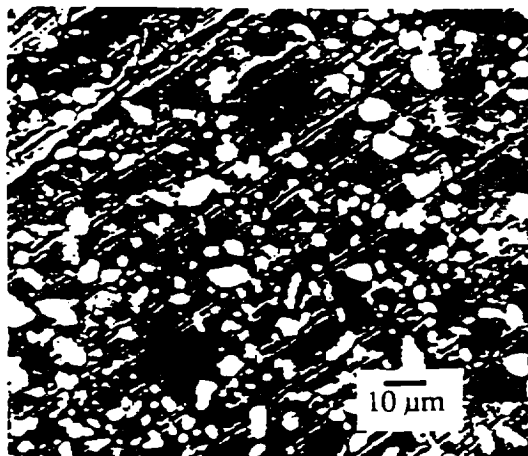
(a) $x = 0.20$, 500 X



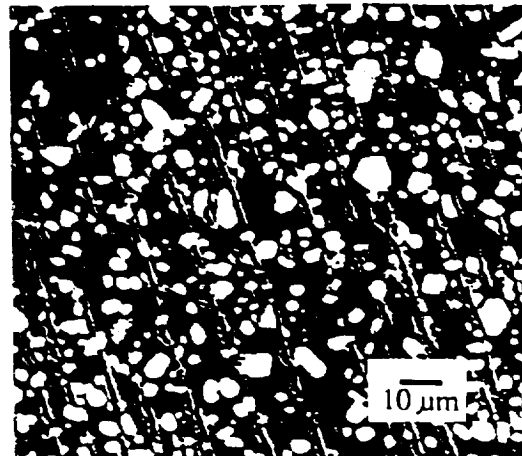
(b) $x = 0.50$, 500 X

SEM micrographs of two Y_2O_3 added samples with $x = 0.2$ and 0.5 respectively.

Fig. II.7a Micrograph of Y123 with Excess Y. Shown here are tiles with no additives, and with Y_2O_3 added at 20% and 50% molar excess of Y.

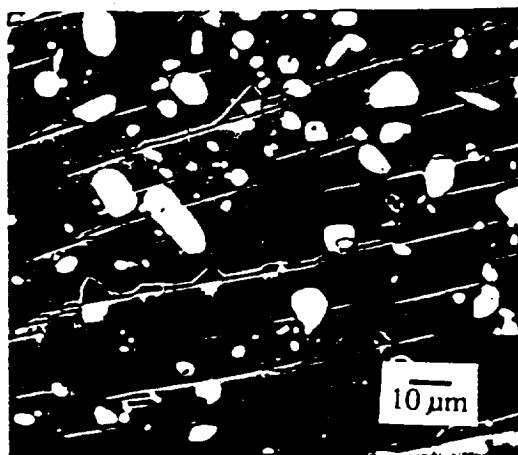


(a) $x = 0.20$, 500 X

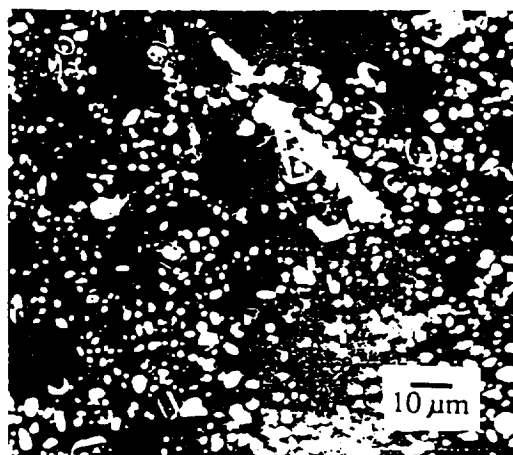


(b) $x = 0.50$, 500 X

SEM micrographs of Y_2BaCuO_5 added samples with $x = 0.2$ and 0.5 respectively



(a) $x = 0.15$, 500 X



(b) $x = 0.30$, 500 X

SEM micrographs of Ho_2O_3 added samples with $x = 0.15$ and 0.3 respectively

Fig. II.7b MT Y123 with added Y211 (20% and 50% molar excess Y) and with added Ho_2O_3 (15% and 30% molar Ho wrt Y in Y123).

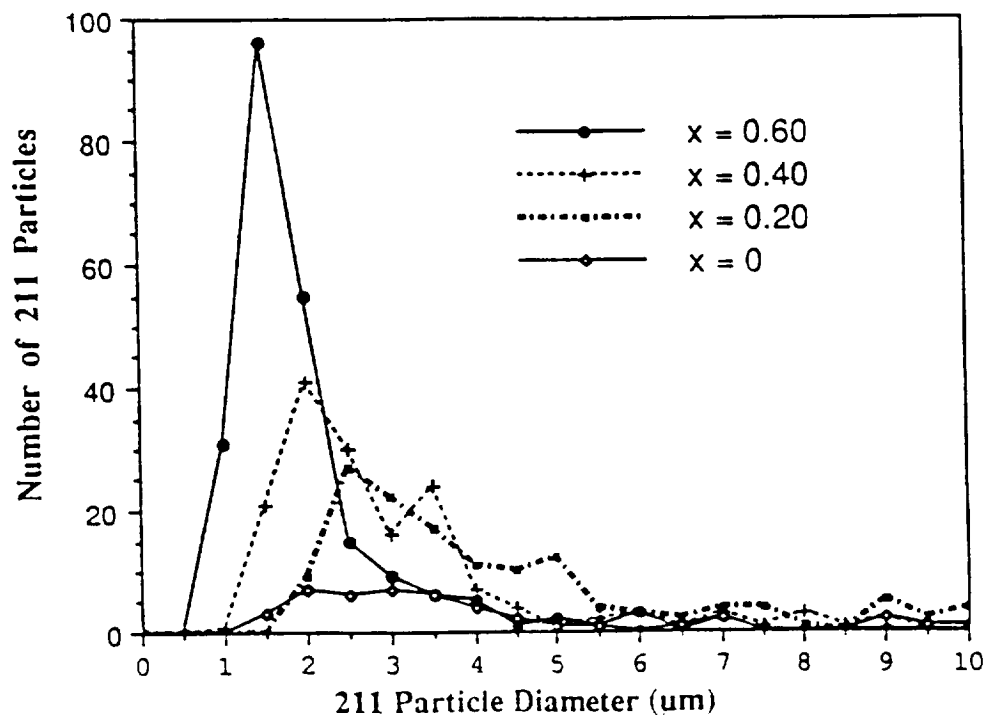
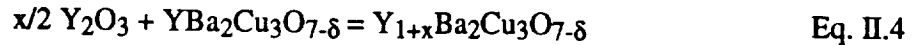


Fig. II.8 Particle size distribution of Y211 with different amount of Y₂O₃ addition.

Other studies show Y211 particle size can be further reduced by adding a small amount of Pt (typically 0.6% by Wt) and using the quench melt growth method⁽¹³⁾. We are pursuing this development.

Some additional detail of our work with excess Y is now given⁽¹¹⁾.

We mix $\text{YBa}_2\text{Cu}_3\text{O}_7$ and Y_2O_3 powders together. Both powders are purchased commercially with a purity of 99.9%. The excess amount of the Y_2O_3 added to the mixture is normalized to $\text{YBa}_2\text{Cu}_3\text{O}_7$ in terms of excess Y molar ratio. It can be represented by the following formula:



The mixture of the powder is then pressed into pellets and sintered at 900° C in air for 24 hours. Next, a typical liquid phase treatment is followed: heating the samples to 1,100° C for 1 h and slowly cooling from 1,050° C to 950° C at a rate of 1° C/h. The sample is typically annealed at 400-600° C for 1 week in flowing oxygen gas.

Based on the phase diagram of Y-Ba-Cu-O system, Y123 has a peritectic transformation at about 1,050° C. Above this temperature, for example 1,100° C, Y123 transforms into Y211 phase and Cu/Ba rich liquid. A sample with excess amount of Y shifts the equilibrium composition to favor Y211 rather than Cu/Ba rich liquid. This shift creates a higher volume percentage of Y211 phase, if the peritectic transformation is completed. Since the Y_2O_3 is not a chemically stable phase at 1,100° C, the Y_2O_3 will most likely react with Cu/Ba rich liquid and form chemically stable Y_2BaCuO_5 (Y211).

A typical characteristic of this material is that two different phases are observed. The superconducting $\text{YBa}_2\text{Cu}_3\text{O}_7$ (Y123) phase has well-aligned crystalline plane orientations, and the small Y211 particles are non-superconducting and randomly dispersed.

Relatively large Y211 particles (about 10-30 μm in size) are observed in stoichiometrically correct Y123. In Fig. II.7 it is seen that the Y211 particle size decreases and the number of Y211 particles increases as the amount of Y_2O_3 addition increased. It is also noted that Y211 particles become more homogeneously distributed. Quantitative analysis of Y211 particle size distribution is shown in Fig. II.8. A relatively low count and wide distribution of Y211 particle size is observed in MT Y123 without any Y_2O_3 addition. A consistent decrease in Y211 particle size and increase in Y211 particle number are observed as the excess amount of Y_2O_3 is increased. The average Y211 particle size for an $x = 0.60$ (60% molar excess Y) sample is about 1.5 μm in diameter.

It would be desirable to produce a final material with no radioactivity above naturally occurring levels. It is with this goal in mind that we continue to study this "chemical" approach to creating pinning centers. The goal is to achieve a magnitude of J_c increased by chemical methods, comparable to those we achieve by radiation methods. At present, even with excess Y, the J_c of MT Y123 which is not irradiated, is only 10,000 A/cm^2 - 13,000 A/cm^2 at zero field, whereas $J_c = 45,000 \text{ A}/\text{cm}^2$ with light ion bombardment (See Sec. II.D and II.F), and $\sim 85,000 \text{ A}/\text{cm}^2$ with heavy ion bombardment (Sec. II.H). The maximum increase in J_c reported as achieved by chemical means⁽¹²⁾ is only 30%, whereas particle bombardment at high energy achieves 370%-850%.

To date, the major result of the study involving excess Y and H_0 has been to increase the grain size, d , and thereby increase the field trapped in an unirradiated single tile to 1,500 G.

After irradiation, the field trapped in a proton irradiated melt textured sample of Y123, with excess Y (i.e., MT Y1₊23) increased to 6,418 G for a single tile, and 14,200 G for a mini-magnet 1.4 x 1.4 x 0.4 cm³, at 77 K⁽¹⁶⁾. Thus the Y study, and Y addition, increased trapped field by a factor of about 3.

F. Second Proton Bombardment, and Bombardment with 3He⁺⁺ and 4He⁺⁺

The measurement mentioned above (14,200 G mini-magnet) was made with material which was bombarded with 200 MeV protons at the Indiana University Cyclotron Facility (IUCF). The previous proton bombardment at Harvard had cost ~ \$2,000. At Indiana, because interest in our work had considerably increased, along with B_t, we were accepted as a visiting experiment and provided free time. The Indiana split beam (parasite running) provided us with 100 - 300 nA of protons, compared with 6 nA at Harvard.

We wanted to uniformly bombard the samples, which now had d ~ 1.4 cm (compared to d ~ 0.5 cm at Harvard). In order to cover the larger, newer samples uniformly, therefore, almost 8 times as much beam was needed as at Harvard. We also wanted to irradiate a larger number of samples, to a higher level. Thus the factor of 50 in intensity available at IUCF was most welcome. The equivalent bombardment at Harvard would have cost \$100,000. Without acceptance of a proposal, as in our case, the bombardment at IUCF would have cost \$8,000. As it is, there were no cyclotron charges for the runs.

In the IUCF bombardments Dr. C. Foster of IUCF joined our UH team.

We spread the beam of the cyclotron from its natural width of 2 mm, to 2 cm, by means of a thin foil scatterer placed about 3 m upstream of the experiment.

In order to study the beam profile quickly and inexpensively, we developed a method of taking "pictures" of the beam, using glass slides. Ordinary glass microscope slides were exposed to typically 100 nc of charged beam. This resulted in a brownish discoloration of that portion of the glass slide which had been in the beam, showing the beam profile. The brown color was known to earlier researchers, and called f-centers (for *farben* *zentrum*). F-centers are electron dense regions which scatter yellow light efficiently. Fig. II.9 shows a typical exposed glass slide.

Fig. II.10 shows the results of the IUCF proton bombardment (black dots). This experiment provides good news which is understood in hindsight, but was not clear at the time. The increase in B_{t,max} as a function of bombardment fluence, F, was experimentally the same for Y1₊23 as it had been for Y123 at the earlier Harvard bombardment. The experiment showed that the increase in B_{t,max} due to irradiation is independent of, and multiplicative with, the increase in B_{t,max} due to excess Y. In terms of more recent understanding, the reason is that irradiation introduces pinning centers and increases J_c, while excess Y increases mainly d. Eq. II.1 predicts (actually postdicts) that J_c and d have independent and multiplicative effects.

Helium

As noted above, we early-on planned bombardment with higher Z projectiles. We proceeded to try bombardment with He when IUCF gave us an extension of running time. In the interim, Civale et al⁽¹⁴⁾ had shown that the J_c of thin single crystals were greatly improved by Sn bombardment. Ionization damage is proportional to Z²/v, and for Tin Z is high enough so that the ionization losses *melt* a column about 100 - 1,000 Å° wide, along the ion track.

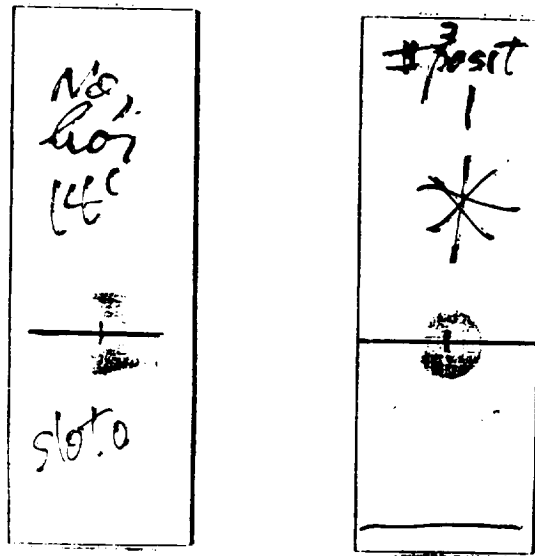


Fig. II.9 Microscope glass slide "photographs" of cyclotron beam, used to exhibit the shape of the IUCF proton beam. Left: beam is blown up by incorrectly set quadrupole. Right well focused beam.

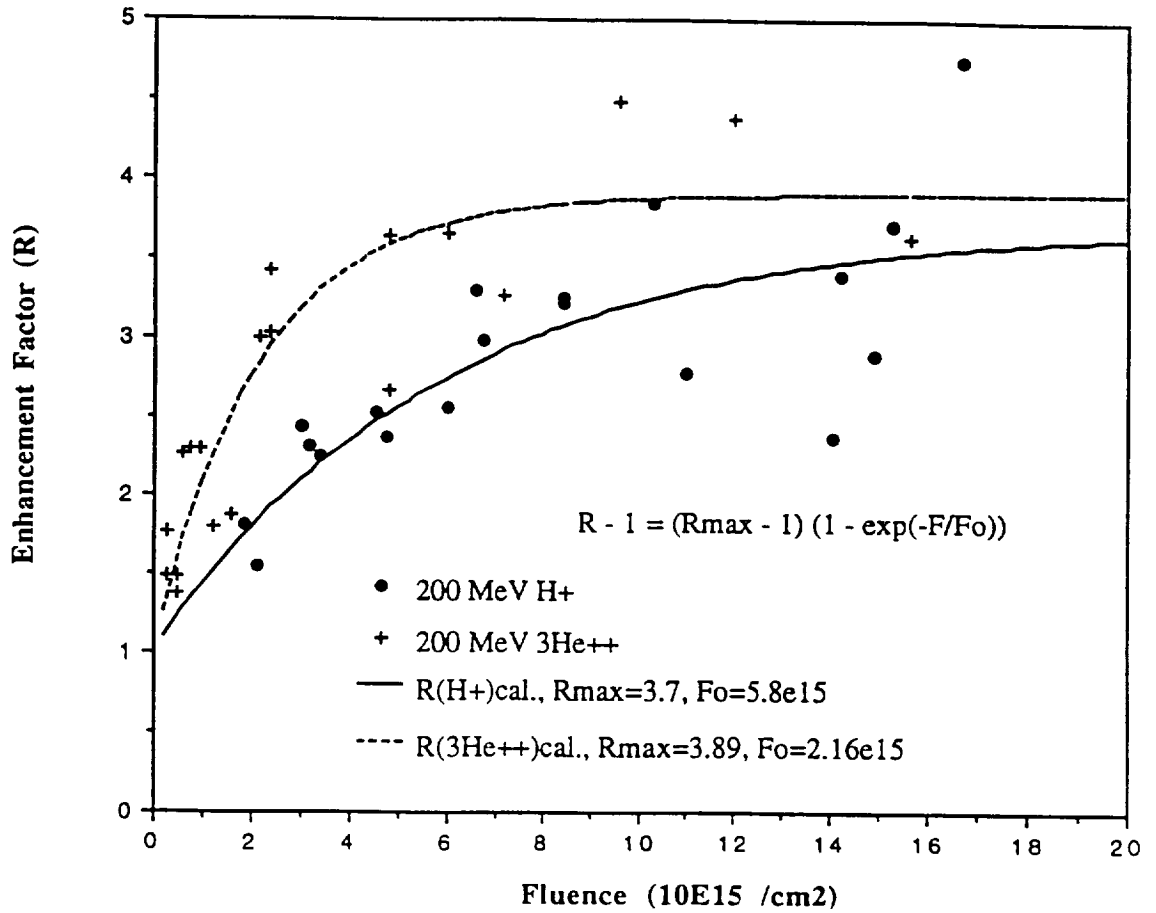


Fig. II.10 IUCF Data on 1H⁺ and 3He⁺⁺ bombardment of Y₁₊₂₃. Enhancement factor $\equiv B_t(\text{after bombardment})/B_t(\text{before bombardment})$ Shown are data on 1H⁺ (dots) and 3He⁺⁺ (crosses) of samples of MT Y(1+23)

At the time that we did our experiment using 3He^{++} , conventional wisdom held that we would get essentially the same results as for 1H^+ . The reasoning was that (a) the nuclear cross sections for 1H^+ and 3He^{++} bombardments are very nearly equal at high energies, and (b) the Z of He is too low to provide ionization losses high enough to result in increased pinning (a column of melted Y123).

The data for the He^3 run is also shown in Fig. II.10 (crosses), along with the data of the previous IUCF proton run. It is seen that the value of F_0 , (as in Eq. II.3) needed to fit the 3He^{++} data, is about 2.7 times smaller than that needed to fit the proton data⁽¹⁵⁾. This came as a surprise.

The nuclear cross sections for 1H^+ and 3He^{++} are essentially equal. In this experiment the ionization energy loss per unit length for 3He^{++} is about 9 times that for 1H^+ . It is clear, therefore, that ionization damage *is* playing a role in the creation of pinning centers⁽¹⁵⁾.

Our proposed explanation of this is that statistical fluctuations in the number of ions created per unit length created by 3He^{++} provides *points* along the 3He^{++} track which do melt, even though the entire track does not melt. The "string of beads" provided by the melted points results in an improved situation for pinning. Hence a lower fluence of 3He^{++} is needed, relative to 1H^+ , to achieve the same increase in J_c .

We plan to continue this experimental direction. We will try bombardment with Li^{+++} and possibly C^{+6} , at the Michigan State Superconducting Cyclotron and, in parallel, we will perform calculations on the string-of-beads model. The Michigan machine will be needed to experiment with $Z > 3$. (There is some chance that $Z = 3$ may be done at IUCF).

G. Increases in d by Chemical and Temperature Gradients

The grains of Y123 which grow from the liquid state usually commence growth at several sites within the melt. Where the growth islands collide, a grain boundary is formed, and that boundary typically is a weak link.

We discuss here two methods of controlled grain growth to reduce the number of growth centers to 1, the use of chemical gradients and temperature gradients.

In the chemical gradient approach we prepare the sample with, e.g., 5 layers. The layers would have varying excess Y of, e.g., 20%, 40%, 60%, 80%, and 100%. We believe that this, in effect, creates the equivalent of a linear temperature gradient, due to the variation in melting temperature. We have experienced some success with such chemical gradients.

The temperature gradient approach is similar. The temperature across the sample is varied, e.g., by $30^\circ \text{C}/\text{inch}$, during the phase in which the grain is growing.

Our best result to date, using combined chemical and temperature gradients has been grains ~ 2 cm in size. Fig. II.11 shows the trapped field on a 2.3 cm sample⁽¹⁶⁾. The field pattern; interpreted by our current model (Sec. III) indicates that the sample is nearly a single grain. The unirradiated tile is seen to trap 2,200 G. To be compared to 1,500 G for a sample made in April 91, whose size was ≈ 1.4 cm. We predict, from Eq. II.3, that the unirradiated 2.3 cm tile, when proton irradiated, will trap 8,140 G.

The results to date on the use of chemical gradients are, in our judgment, limited.

Melt-Textured Y-Ba-Cu-O Sample Processed by
Chemical Gradient Method (Y gradient)

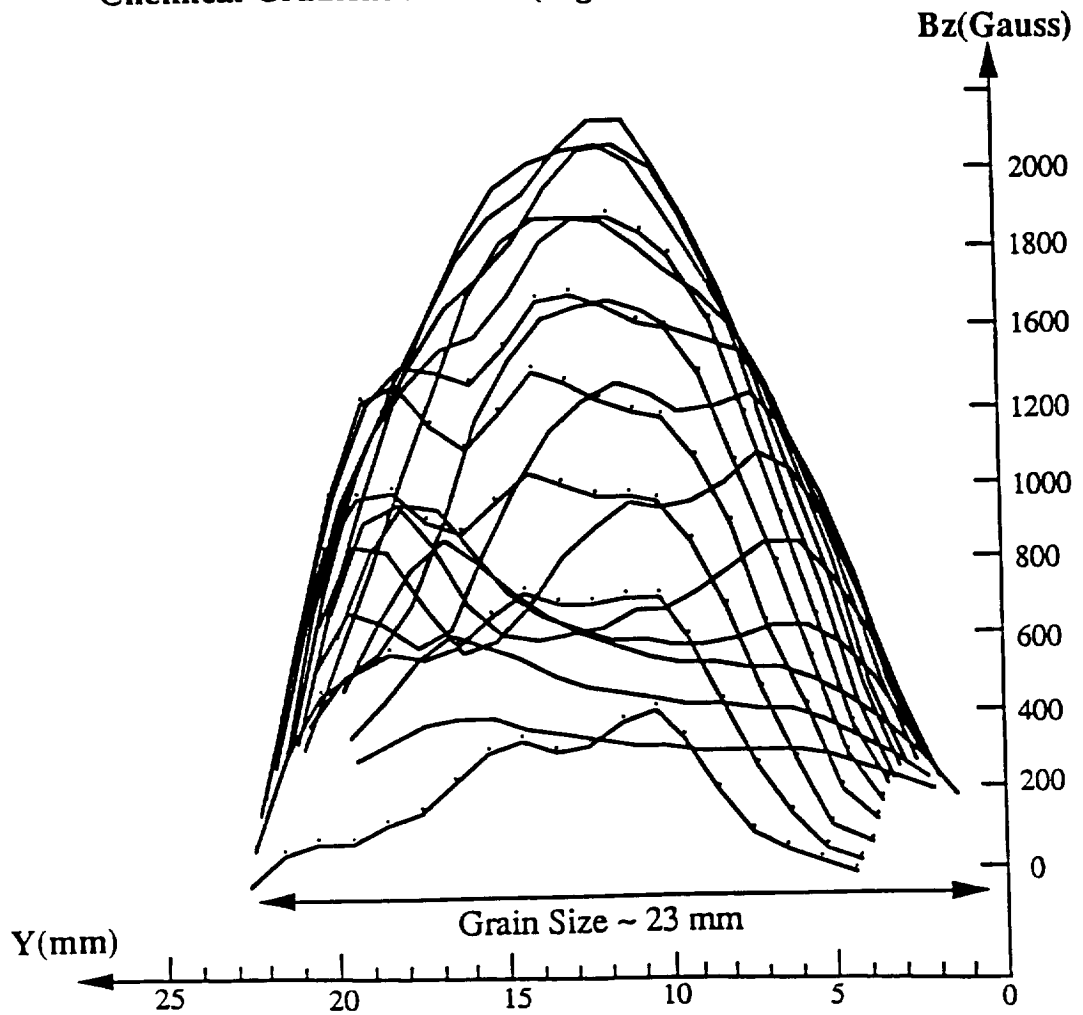


Fig. II.11 B_t Across Face of 2.3 cm Y_{1+23} tile, in x,y plane (a,b crystal plane).

The use of temperature gradients is promising, but very difficult. Heat or cooling is applied only to the surface of the sample. However, the heat of fusion is released as a volume effect, throughout the sample. Thus, simple temperature gradients are difficult to obtain.

We will continue this work. However, groups larger than ours are devoting massive manpower efforts to the temperature gradient approach at Boeing, Nipon Steel, and ISTEAC.

We have done some initial work using seed crystals to predetermine the growth direction. We consider the early results very promising and plan to continue our study of seed crystals.

H. High Z Irradiation

As noted above, it was clear some time ago that high Z bombardment should be explored. The work by Civale et al⁽¹⁴⁾ made that even clearer. Civale's approach was bombardment by a beam of high energy Sn ions, whose penetration depth was only a few microns. Such bombardments are expensive, and many bombarded samples would be needed to build up enough Y123 material to fabricate devices. However, Civale's work clearly demonstrated advantages of columnar defects.

We considered several ways to simulate the damage centers produced by high energy, high Z ions including mechanical, chemical, and radiation approaches. We finally elected to experimentally try an approach in which we would create damage "tubes" of about the diameter of Civale's Sn ions, but with a much greater depth penetration. However, the direction (axes) of the tubes would be isotropic.

We adopted a method pioneered by GE⁽¹⁷⁾, in which U is added to Y123. GE's work was limited to sintered material, and extrapolation to melt textured Y123 is not trivial, nor assured, because the U can effect melt texturing.

Only depleted U was available to us, with a U²³⁵ fraction of only 0.45%. With this we made batches of Y1₂₃, including U content of 0, 0.15, and 0.6%. Samples from each of these batches were exposed to thermal neutrons. n° irradiation fluences of 7.2×10^{16} , 4.3×10^{17} , and 2.6×10^{18} were used.

Fig. II.12 shows the results of the first experiment. (The second experiment is presently in progress.)

The experiment involved new chemistry which resulted in uneven initial results in the melt texturing. In addition, the n° bombardment was done at the Texas A&M reactor, which has a sizable fast neutron component. Also, the U tended to cluster in deposits smaller than, but of the order of the range of fission fragments. Some conclusions can be drawn despite the lack of control of these variables.

1. A positive effect of the U is seen.
2. The improvement in J_c increases with the U content.
3. The improvement in J_c increase with the neutron fluence.
4. This method provided the highest J_c achieved by our group at 77 K ($85,000 \text{ A/cm}^2$).
5. This method results in about two orders of magnitude lower radioactivity than 1H bombardment.

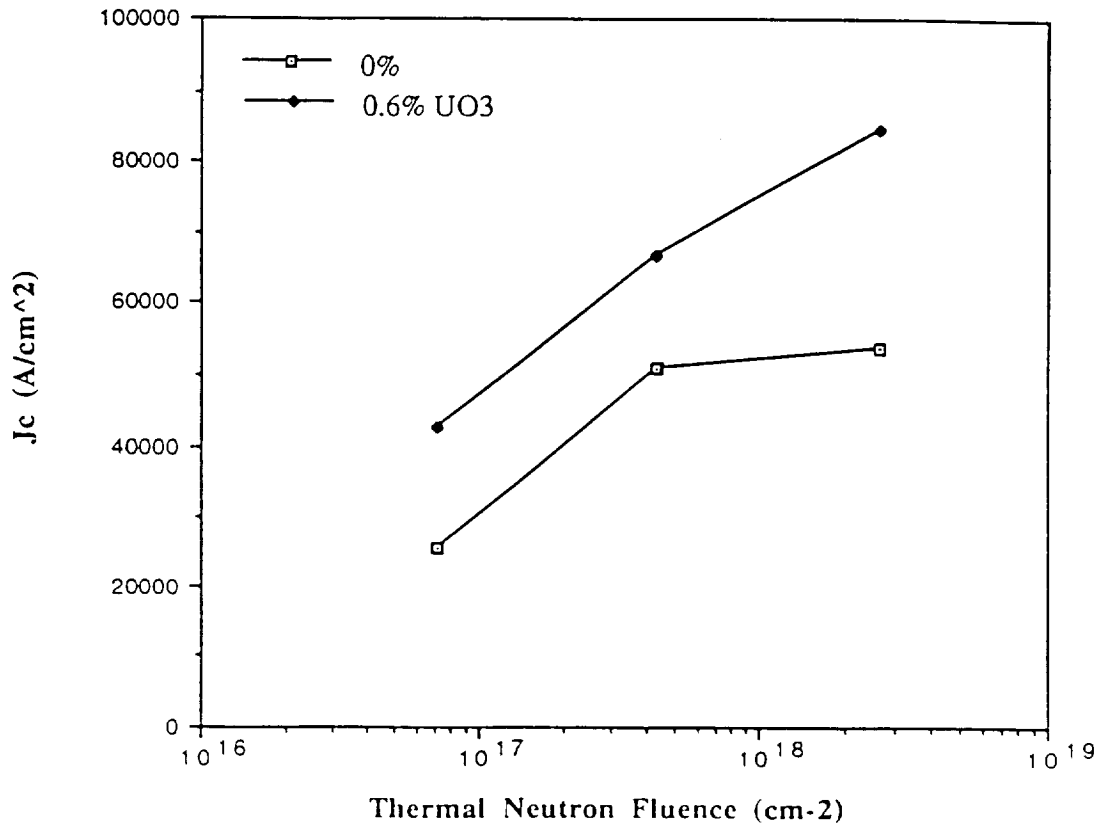


Fig. II.12 Results of neutron irradiation of n/U Y(1+23).
 (Before n irradiation J_c was 10,000-13,000 A/cm²)

We have not yet fabricated a mini-magnet from this higher J_c material because an insufficient number of samples is available. The U content appears to have very little detrimental effect on grain size.

We plan to continue work on U bombardment, including insertion of more U, use of enriched U, dispersion of the deposits of U, and studies of creep.

I. Achievements and Predictions at 77 K

A study was done on our unirradiated MT Y_{1+23} material by Dr. YanRu Ren, at the University of Southampton, U.K. (Dr. Ren has since joined our group at U.H.) Fig. II.13 is one of the results from that study. The data gives J_c as a function of applied field, B_A , with temperature as a parameter. The two temperatures shown are those which can be achieved with liquid nitrogen (a) at atmospheric pressure (77 K), and (b) under vacuum (65 K).

At 77 K it is seen that the current decreases markedly for applied fields in the region $4 T \leq B_A \leq 6 T$.

Y_{123} material with trapped field effectively exists in an applied field equal to its own self field, B_t . Thus it is expected that the ultimate limit of trapped field in a Y_{1+23} quasi permanent magnet, as set by present materials, will be about (5 ± 1) Tesla.

We have to date achieved trapped field of 1.52 T in mini-magnet prototypes⁽¹⁸⁾ at 77 K, using light ion irradiated MT Y_{1+23} , of area approximately $1.2 \times 1.2 \text{ cm}^2$ in the a,b plane. (Because tiles, added along the c axis, by lamination, behave as a single tile, only the diameter, d, of the a,b plane provides a limit.) The thickness of this mini-magnet, made of 8 tiles, was 1.5 cm. The J_c for the samples used averaged about $45,000 \text{ A/cm}^2$ at 77 K.

We have since developed better materials. As reported in Sec. II.H, neutron irradiation of U loaded MT $Y_{1+Ba_2Cu_3O_7}$ (we will denote this as $n^{\circ}/U Y_{1+23}$) has resulted in $J_c \approx 85,000 \text{ A/cm}^2$. Thus, if tiles of the same size as used in the 1.52 T mini-magnet, but U loaded, are manufactured and neutron bombarded, the predicted field is $B_{t,max} = (85 \text{ kA/cm}^2)/(45 \text{ kA/cm}^2) \times 1.52 \text{ T} = 2.87 \text{ T}$. We plan to produce, and fabricate such tiles into a mini-magnet in the near future.

By means of chemical and temperature gradients the a,b plane size has been increased to 2.3 cm, as reported in Sec. II.G. The process of producing tiles with $d > 2 \text{ cm}$ is still not well controlled, and predictions based on increased d are less subject to a timetable than are bombardment studies.

When we can reliably produce 2 cm tiles, $f(d)$ (of Eq. II.1) predicts trapped field increase by a factor of ~ 1.4 . Thus the expected trapped field in a mini-magnet with $d \sim 2.3 \text{ cm}$, composed of $Y_{1+Ba_2Cu_3O_7}$, and irradiated with $1H^+$ or $3He^{++}$ is expected to be $1.4 \times 1.52 \text{ T} = 1.75 \text{ T}$.

The U loaded melt textured materials we have produced ($n^{\circ}/U Y_{1+23}$) appear to be of quality comparable to Y_{1+23} without U. We may thus make one final prediction. A mini-magnet composed of $n^{\circ}/U Y_{1+23}$, with $d \sim 2.3 \text{ cm}$, will have a field of $(85 \text{ kA/cm}^2)/45 \text{ kA/cm}^2 \times 1.4 \times 1.52 \text{ T} = 4.0 \text{ T}$ at 77 K.

We conclude that the materials and processes we have developed to date may reasonably be expected to trap values of B_t of 4.0 T, at 77 K, close to the limiting achievable field of Y_{123} .

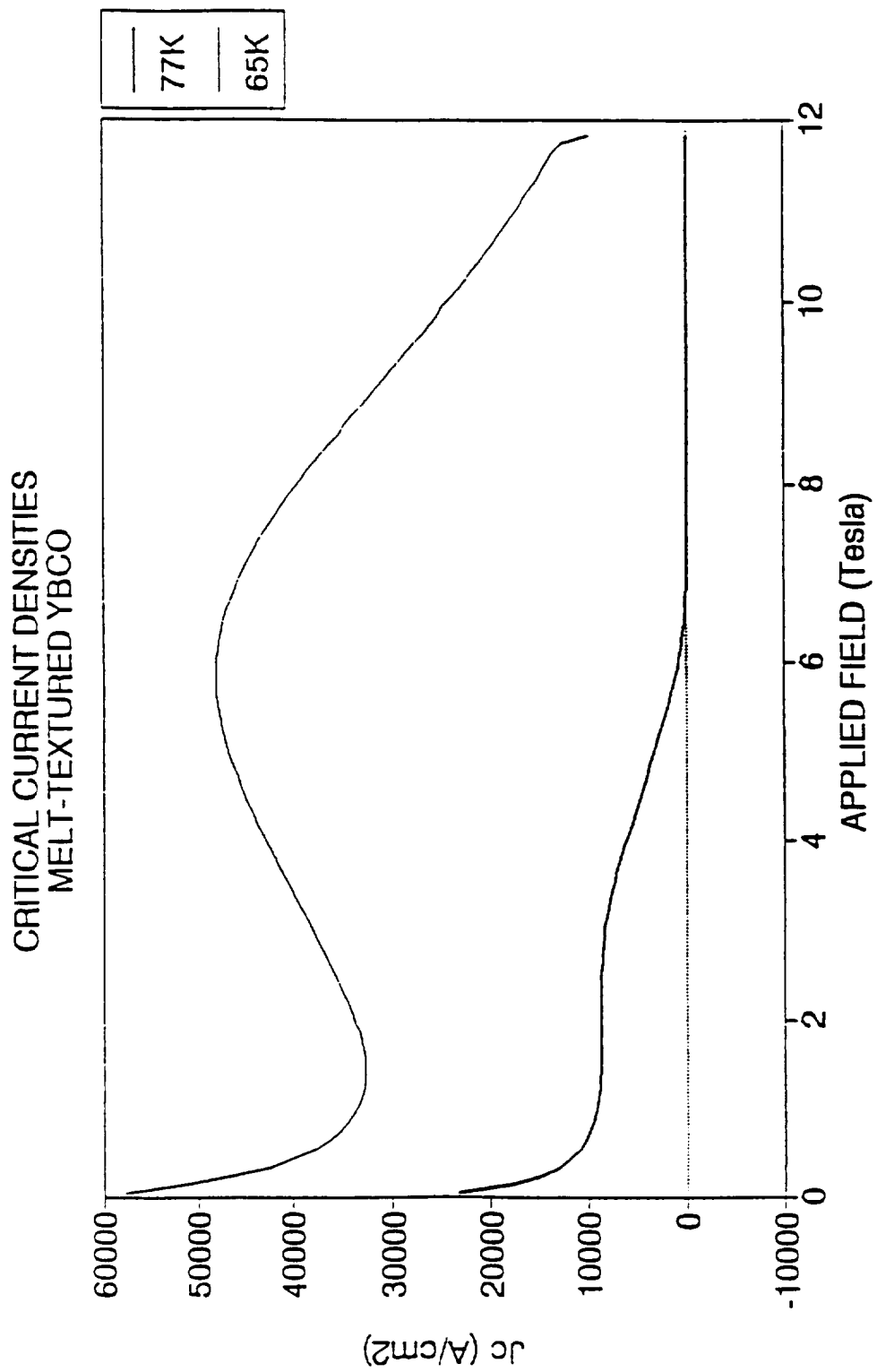


Fig. II.13 J_c vs. B_A at 77 K and 65 K. Data of Y. Ren, Univ. of Southampton, U.K., on a UH melt textured sample.

J. Temperature Dependence

In 1990 we did our first test below 77 K. A Y1₊23 mini-magnet, not irradiated, was field cooled in liquid nitrogen, under vacuum. The temperature was ~ 65 K because of the vacuum. An increase in field trapping ability from 3,016 G to 8,587 G was observed.

Since that time our group has desired to activate irradiated samples at lower temperatures. Two obstacles prevented this.

First, our highest field laboratory magnet was a 2 T iron electromagnet. We had a refrigerator fitted to this magnet, capable of reaching 10 K. However, the magnet could not provide the activating field, B_A , needed to activate the samples to the maximum field they could trap.

Results such as those shown in Fig. II.14 were obtained. A rapid rise in B_t is seen, until B_t approaches the limiting field of the electromagnet (1.95 T in the case of Fig. II.14). In the experiment shown in Fig. II.14, $B_t \approx 1.9$ T was achieved. However the data does not separate the effect of limited B_A from that of limited B_b or J_c .

In the Fall of 91, an old 10 T, low temperature superconducting magnet was provided to our Institute on long term loan. The magnet was in bad shape (leaks, damaged gaskets, inoperative power supply, non functioning vacuum system). It took until Fall 92 to get it operating.

During the period of repair multiple attempts were made to arrange use of high field large volume, controlled temperature activation magnets in the possession of other groups, but none succeeded.

Once the 10 T magnet was working, we could at last provide enough applied field to reach $B_{t,max}$ at lower temperatures. However, our refrigerator temperature sensor will not work in the 10 T magnet, due to the high field. Thus we lack the ability to lower T. We are now producing a cryostat system compatible with the 10 T magnet.

In the interim, we ran an experiment at 64.5 K. This temperature was, as in the earlier experiment, achieved by cooling with liquid nitrogen (77 K), and then pumping above the liquid nitrogen to reduce its temperature to 64.5 K. In this way data were taken at 64.5 K on the same mini-magnet which trapped 1.52 T at 77 K.

Fig. II.15 shows data on the mini-magnet at 77 K and 64.5 K.

Each point in Fig. II.15 represents a field cooled data point. Between data points the magnet was warmed to $T > T_c$, and then cooled again at whatever applied field was desired. The magnet was then removed from the field, and B_t was measured.

The result at 64.5 K was $B_{t,max} \approx 3.96$ T⁽¹⁸⁾.

To the best of our knowledge this is the highest quasi-stable field ever achieved by any means.

In particular, the result exceeds the field of 2.3 T achieved by Rabinowitz et al⁽¹⁻³⁾ using low T_c superconductors at liquid helium temperature, a record which stood for almost 20 years.

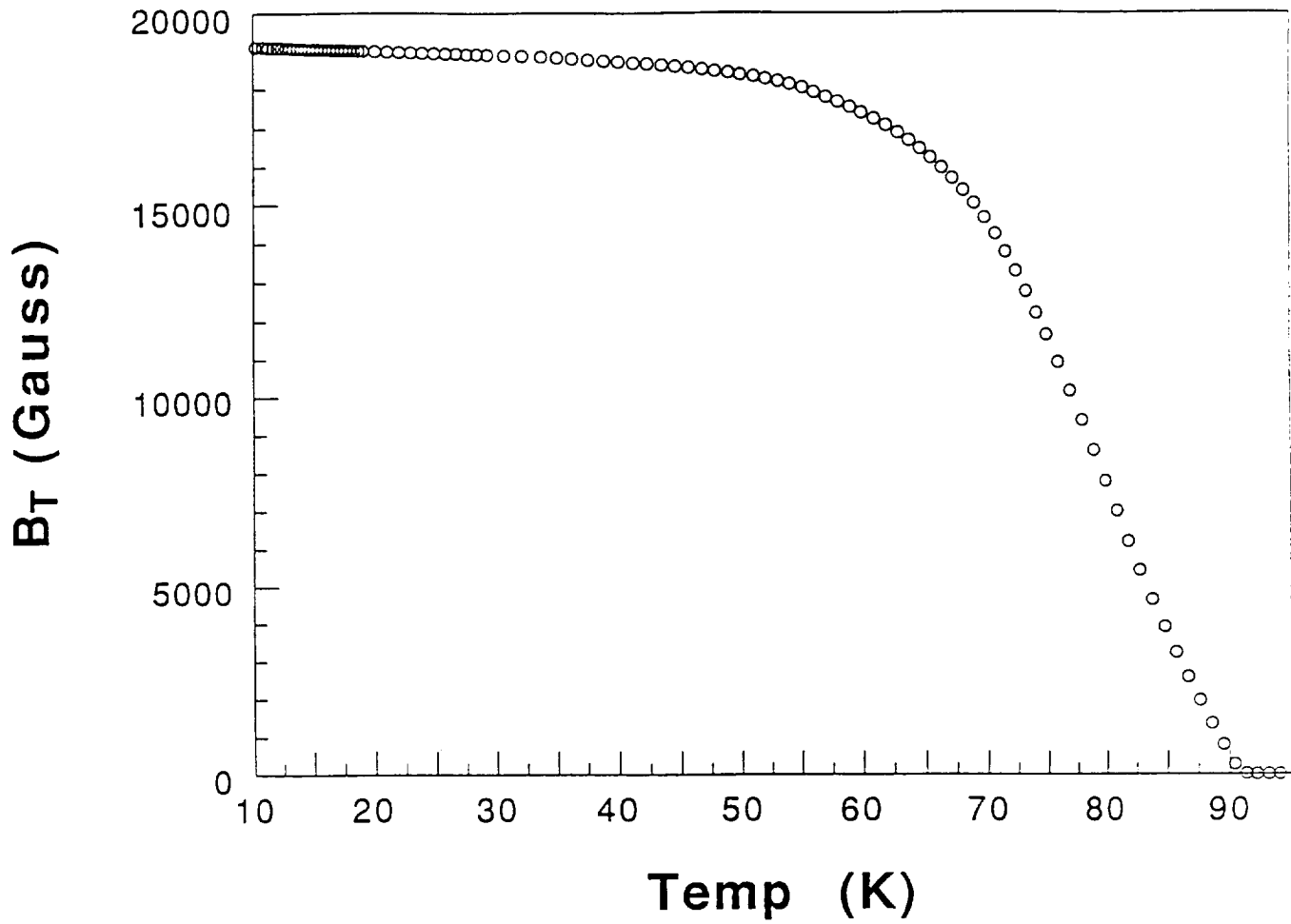


Fig. II.14 Temperature Dependence of Trapped Field and/or J_c . The maximum trappable magnetic field is shown as a function of T. The activation field, for this data, was limited to about 19,500 G. (A 100,000 G activation magnet has since assembled.)

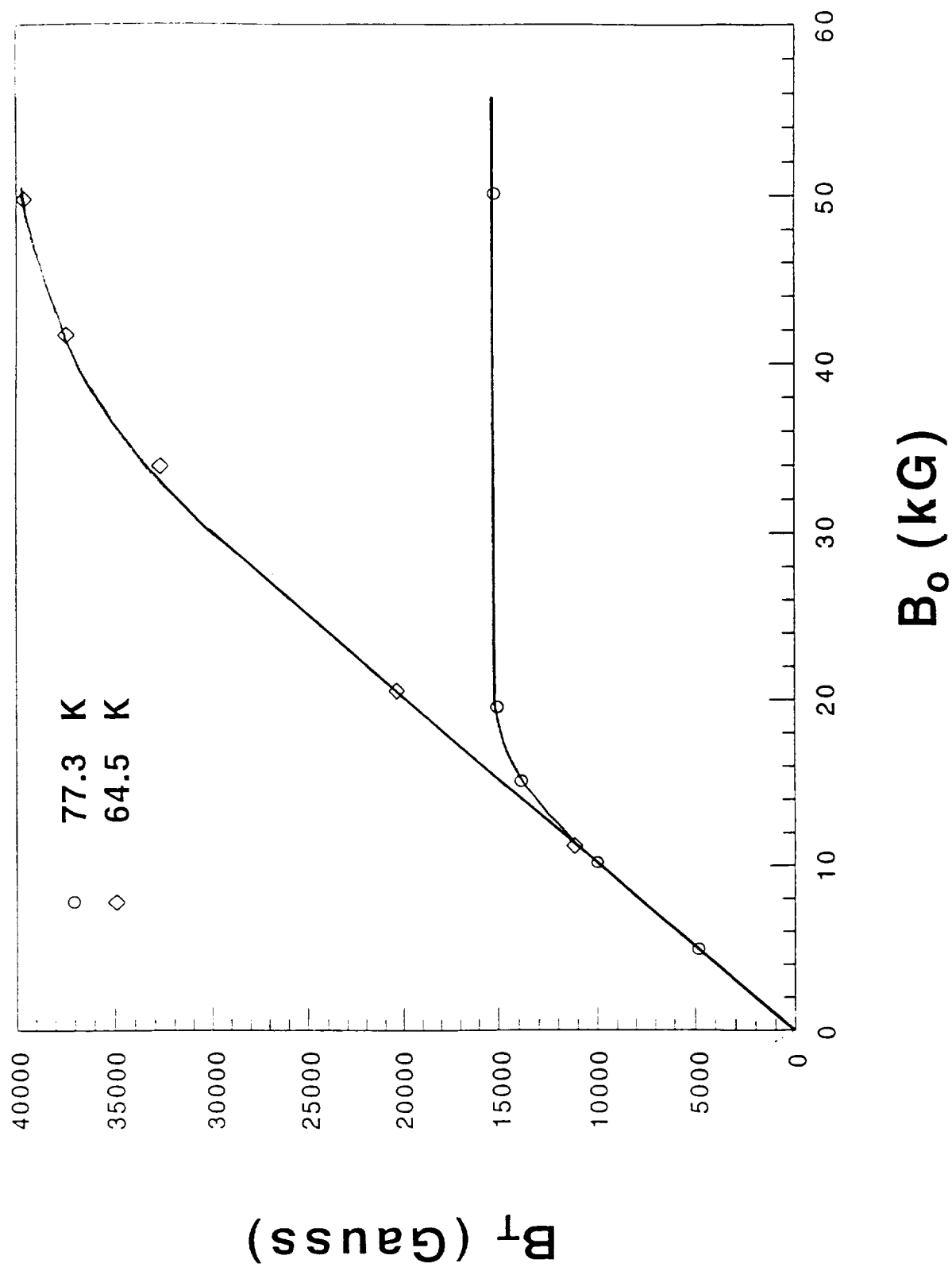


Fig. II.15 Activation curves for a mini-magnet of MT Y(L-23), bombarded with light ions. $B_{t,max} = 15,250$ G at 77.3 K. $B_{t,max} = 39,600$ G at 64.5 K.

During the period when the repair of the 10 T magnet delayed experimental temperature studies, we also expended efforts to *calculate* the effects of temperature.

As noted earlier, Fig. II.13 includes data on J_c vs. B_A at 65K. More recently, in collaboration with a group from Wright Air Force Laboratory, our group extended the study of J_c (T, B_A) to temperatures down to 20 K, and to fields of up to 6 T, using a small aperture high field magnet at Wright Field. Fig II.16 shows the experimental results. J_c is about a factor of 50 higher at 20 K than at liquid nitrogen temperatures.

For any magnet made of the material studied, one can calculate directly from Fig. II.16 the expected field as a function of T , given one starting point $B_{t,max}(T_1)$. In particular, given $B_{t,max} = 1.52$ T at 77 K, for the mini-magnet described above (or given $B_{t,max} = 3.96$ T at 64.5 K) one can use Eq. II.1 to calculate $B_{t,max}$ at any T , assuming that the magnet will be subject to only its own self field.

A more illuminating, albeit more limited, calculation may be done⁽¹⁹⁾. We first learned that, for $B_A < 10$ Tesla and $20 \text{ K} < T < 65 \text{ K}$, a very simple empirical law obtains⁽¹⁹⁾ from the data of Fig. II.16.

$$J_c(T_2) = J_c(T_1)[(T_i - T_2)/(T_i - T_1)]^2 \quad \text{Eq. II.4}$$

The data of Fig. II.16 is replotted to exhibit this behavior in Fig. II.17.

In this equation, T_i is the experimental intercept temperature at which $J_c = 0$. We find that the data, when applied to single grains, produced in our laboratories, is always in agreement with $T_i = T_c$.

Eq. II.1 plus the empirical behavior of J_c represented by Eq. II.4, yields

$$B_{t,max}(T_2) - B_{t,max}(T_1)[(T_c - T_2)/(T_c - T_1)]^2 \quad \text{Eq. II.5}$$

for $20 \text{ K} \leq T_1, T_2 \leq 65 \text{ K}$, and $B_A \leq 10$ Tesla.

Applying Eq. II.5 to the mini-magnet which traps 3.96 T at 64.5 K, we predict (with the caveat that the magnet does not crack under magnetic pressure, or suffer the onset of giant flux jumps⁽²⁰⁾) that $B_{t,max}$ at 20 K will be 27 T!

We are reasonably sure that cracking will be encountered below this value of B_t . Also, the onset of giant flux jumps is assured at liquid helium temperatures⁽²⁰⁾, but we have not yet calculated exactly where it will set in. However, there is a significant literature⁽²¹⁾ on the control of giant flux jumps. Also, cracking can be controlled by admixtures to the Y123 melt (e.g., 15% Ag), and by cladding. These questions remain for future studies.

Purely for amusement we note the following. If a mini-magnet is constructed with our largest present value of $d \sim 2.3$ cm, and $J_c \approx 85$ kA/cm² (the value observed in n^o/U Y123) then the expected field at 64.5 K is $(3.96/1.52) \times 4.0$ T = 10.4 T. If we apply Eq. II.5 to this field, we predict a field at 20 K of $B_t = 71.3$ T!

Of course if still higher fields are desired, they may be available at liquid helium temperatures, or larger values of d .

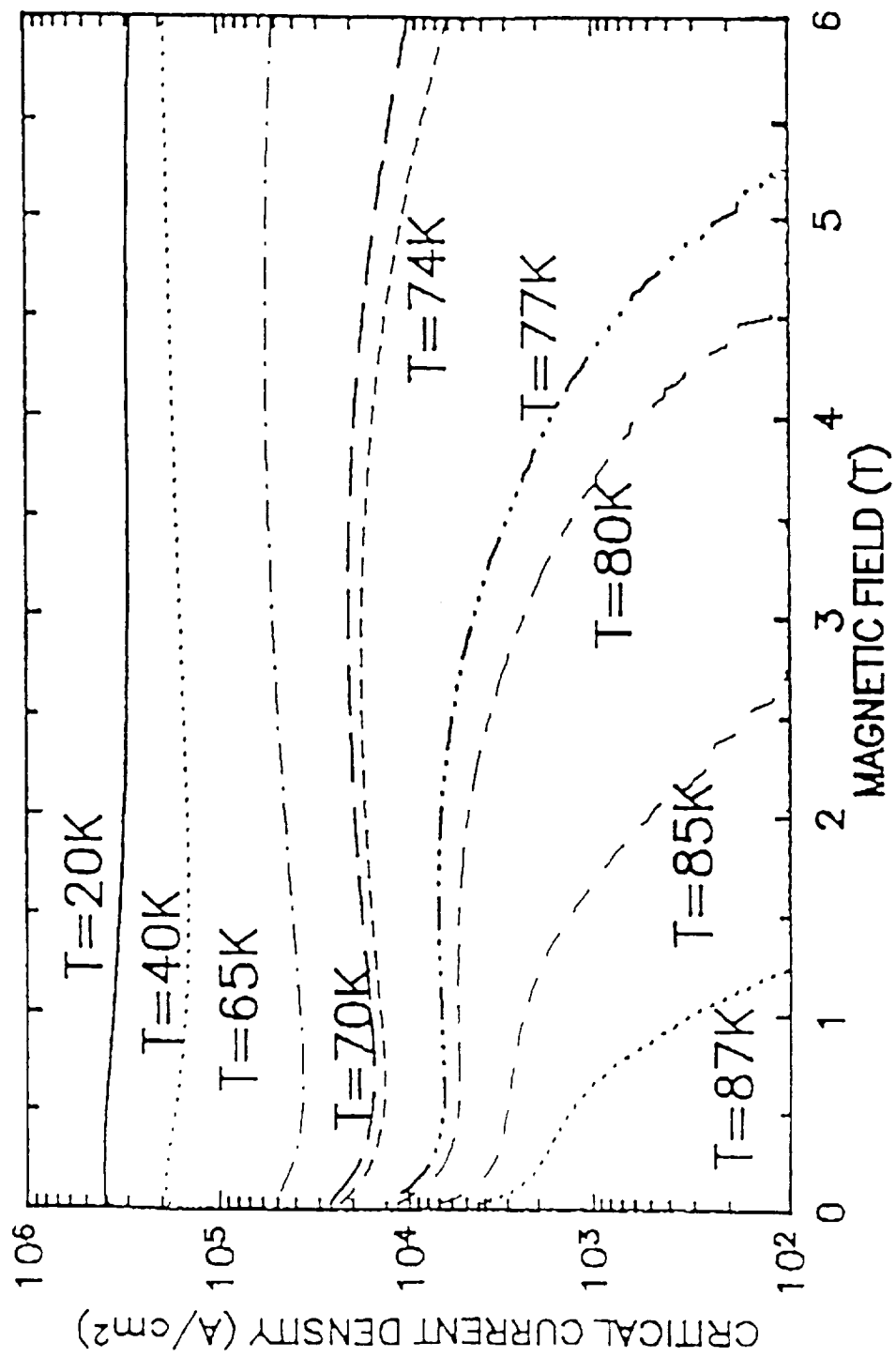


Fig. II.16 $J_c(B)$, with T as a parameter, for a sample of unirradiated $\text{MT Y}_{1.2}\text{B}_2\text{Cu}_3\text{O}_7$

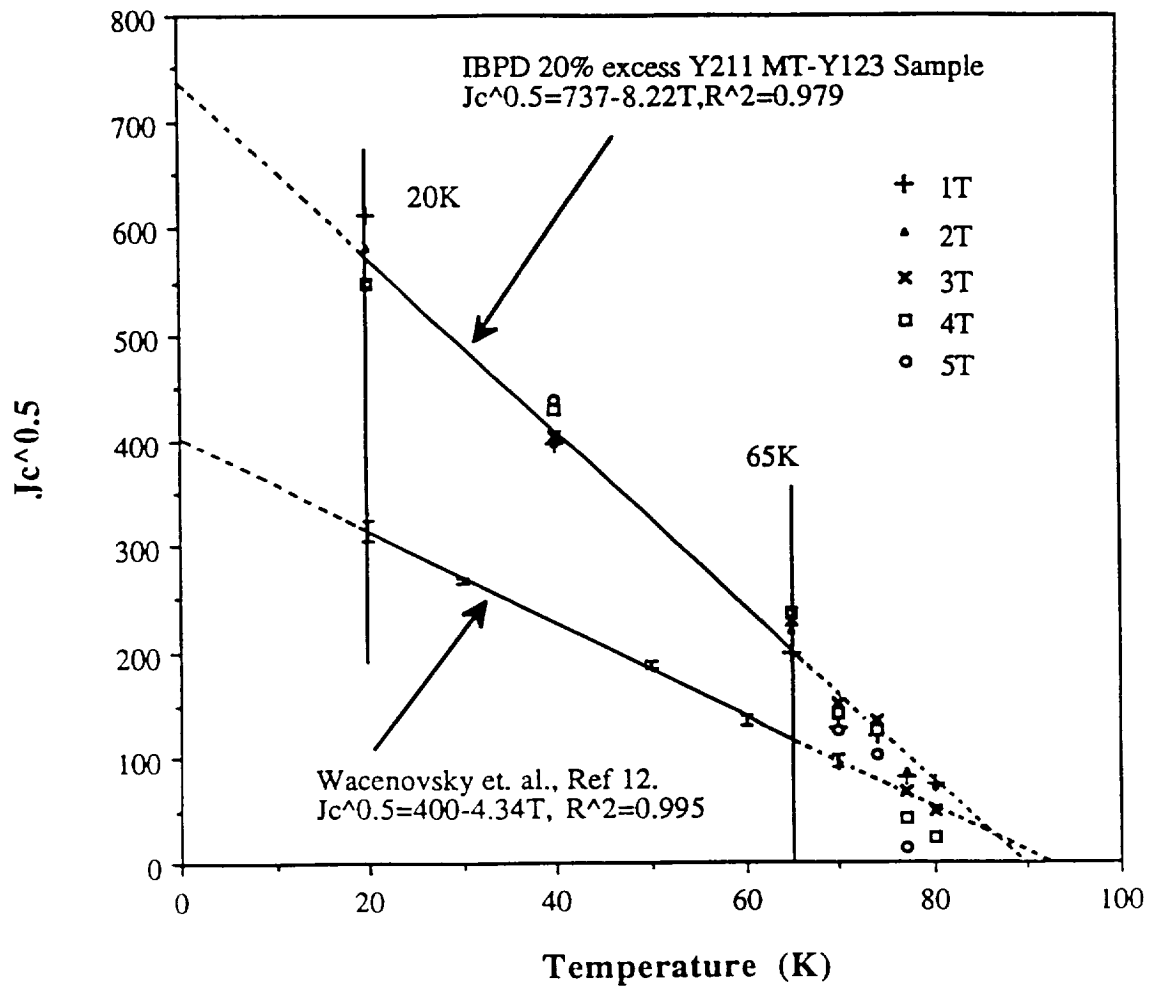


Fig. II.17 $J_c^{1/2}$ vs. T , with B_A as a parameter, for unirradiated Y1+23. This is data of Fig. II.16 replotted as $J_c^{1/2}$ vs. B (top line). For $20 \leq T \leq 65$ K, and $B < 10$ T, a straight line is a good phenomenological fit to the data. Lower curve is data on a sample of Murakami (ISTEC) replotted by us.

K. Conclusions Concerning Magnitude of B_t

At 77 K, $B_t = 1.52$ T has been achieved. Using the n°/U technique for introducing pinning centers, and using $d \sim 2.3$ cm, which has been achieved, fields of 4.0 T are achievable. There is still apparently room to improve J_c and d , and it appears very probable that $B_t \sim (5 \pm 1)$ T will be achieved at 77 K. This is near the irreversibility point (B, T) for Y(123) at 77 K.

Further work on bombardment of Y123 with $Z \geq 3$ is desirable in order (a) to learn more about tailor made pinning centers, and (b) to reduce bombardment flux, and thereby residual radioactivity.

Further work on the n°/U technique is desirable in order (a) to increase J_c , (b) to study the effect of isotropic columnar damage, and (c) to reduce radioactivity.

Further work is also desirable on chemical techniques to replace radiation induced pinning centers with chemical pinning centers. Creep studies should follow each variation in pinning center production.

At lower temperatures, $B_t \sim 4.0$ T has been achieved (at 64.5 K). Fields of the order of 100 T appear to be possible at temperatures of the order of 10 K. For a trapped field magnitude above 4 T, and probably, below 10 T, cracking will set in due to magnet pressure (which is proportional to B^2). Further work is desirable to determine the cracking point. Following this additives, such as Ag, and cladding studies are desirable to increase the mechanical stability.

Sec. III. Two Component model of J_c

A. Field Plots

From the outset of our work we measured trapped field, since high field is a major goal. Field plotting became a very time consuming task in our laboratories as we produced larger quantities of material. We therefore automated our field plotting technique including computer readout of magnetic field, and computer control of the position of the Hall probe. Computer controlled motors, for example, move the Hall probe in an x,y traverse of a sample, at fixed z. The steps in x and y are chosen by the operator. Typically a measurement is made every 1 mm. Studies were made on the hysteresis and vibrational noise, and designs were modified until very reliable results were obtained. Fig. III.1 is a graph of the trapped field of a single grain sample, vs. x and y in the a,b plane, at a fixed value of z, in the c direction.

B. Current Model

We found that when the sample traps $B_{t,max}$, all of our measured results of trapped field can be fit by a surprisingly simple model of the current flowing in the sample⁽²²⁾. Two components of the current are assumed. One is a surface current, J_s . This current is the same as that shown by Ampere to represent a ferromagnet of constant magnetization per unit vol. The second current is a uniform volume current, which circulates in the sample around the line of highest field. Fig. III.2 shows these currents schematically.

Fig. III.3 shows data from field measurements, compared to calculations from this current model. The Hall Probe is moved in the a,b plane. It is seen that the fits are very good. In the fitting procedure only the magnitudes of J_c and J_v are varied. All other inputs are taken from the dimensions of the samples. Two data points are sufficient to fix J_s and J_v , and from this dozens of data points are well fitted. Thus, the model is highly predictive, and it is not simply a parametric fit.

The model was tested on the measured field distributions of two SuCo magnets, and fit very well (see Fig. II.3). It then was used for sintered, melt-textured and irradiated samples (Fig. II.4). It is a good fit, and a sufficient model in all cases. In the case of sintered samples the many small grains, joined by weak links, result in many localized vortex currents. This is exactly the condition for an Amperian current such as J_s , to validly represent the magnetic field. Indeed we find that for sintered samples, and for SuCo magnets, the best fit involves J_s only. The best fit value of J_v is zero.

The most popular current model for *single* grains of HTS and for low T_c materials, is the Bean model⁽²³⁾. Our model is equivalent to the Bean model if we set $J_s = 0$. However, the J_s term is required for a good fit. Fig. III.4 shows field measurements across the diameter of the a,b plane. The solid line is the prediction of the J_s+J_v model, when a best fit is obtained. The agreement is good. The dashed lines are fits with $J_s = 0$. These fits are far outside experimental errors (which are about 1%). While the disagreement is not dramatic, it is a bad fit. Such bad fits are characteristic of any fit on a large grain obtained with $J_s = 0$. In Sec. III.E we shall discuss an extension of the J_s, J_v model to the unsaturated case, where much more dramatic failures of the Bean model occur.

Thus, in the case of melt-textured samples activated to $B_{t,max}$ (the so called saturated or critical state) both J_s and J_v are required for a good fit. So far, in our experience, as the melt-textured sample increases in size, the ratio J_v/J_c increases.

While the Bean model⁽²³⁾ can not fit the data, the Kim-Bean model⁽²⁴⁾ can. The Kim-Bean model, which is a successful physics model of the currents in a saturated (critical state)

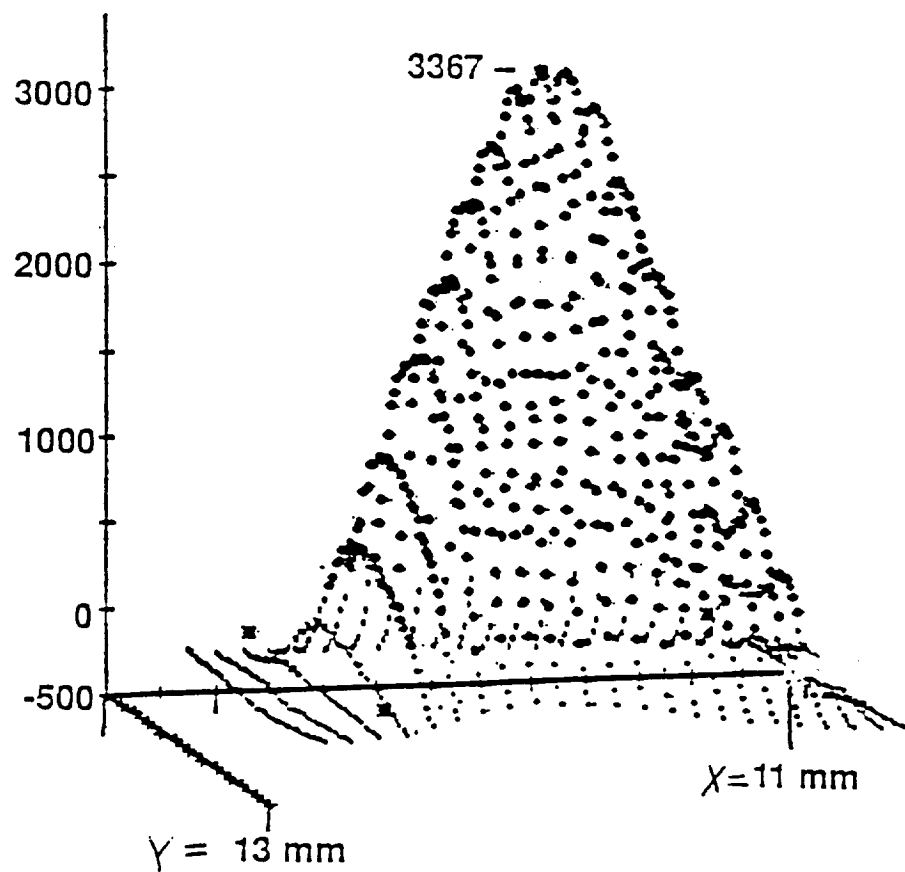


Fig. III.1 Field Map, $B_t(x,y)$. Automated data taken on single MT Y1+23 tile, p^+ bombarded. B_z (along c axis) is plotted vs. x,y (in the a,b plane).

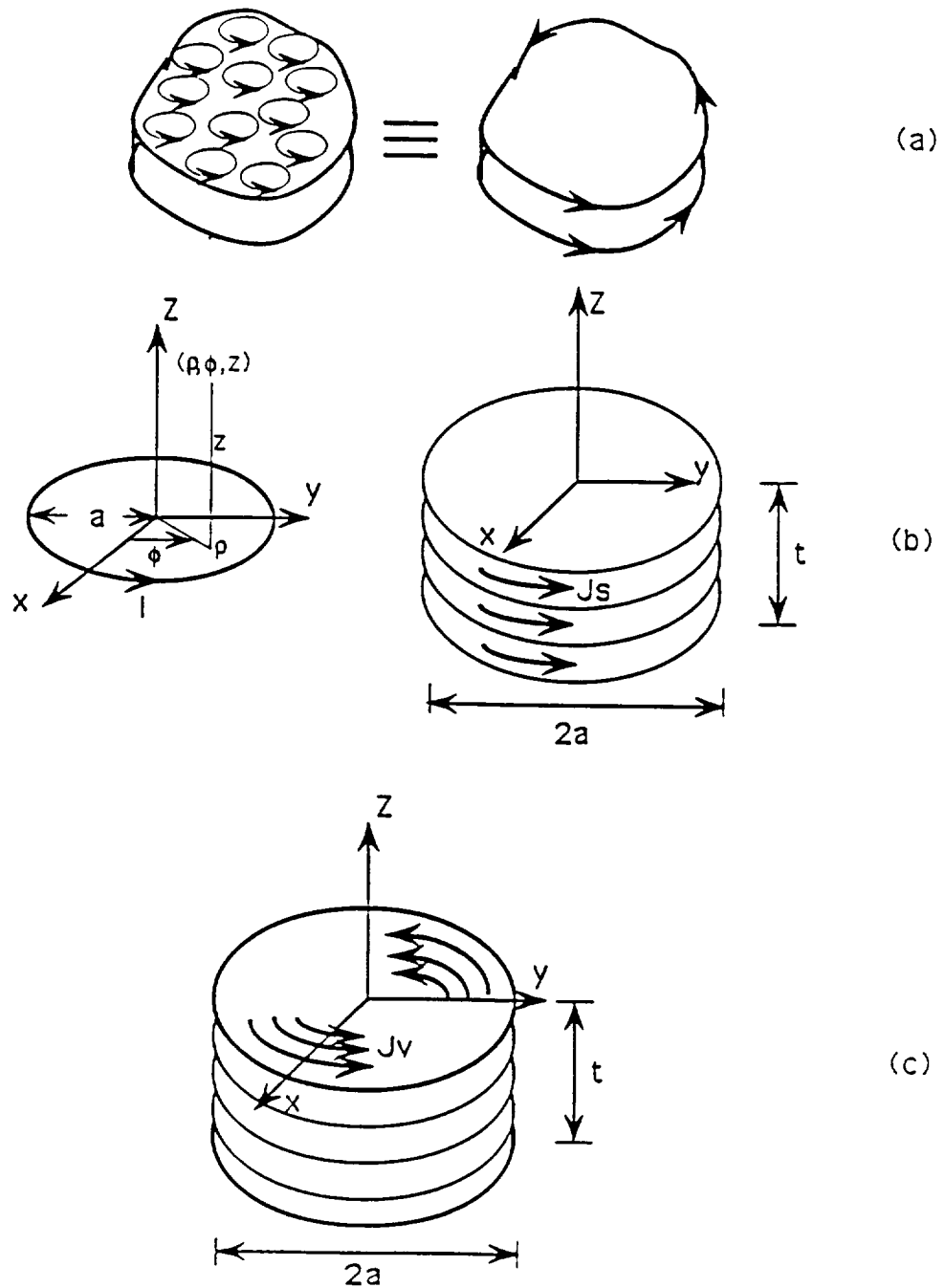


Fig. III.2 Schematic of two current model. Shows constant surface and volume currents. (a) Vortices represented by Amperian current. (b) Coordinates used in integration, and schematic of J_s , for B_t along Z direction. (c) Schematic of J_s . Note $a \equiv$ radius of sample d (as used in this report) $= 2a$.

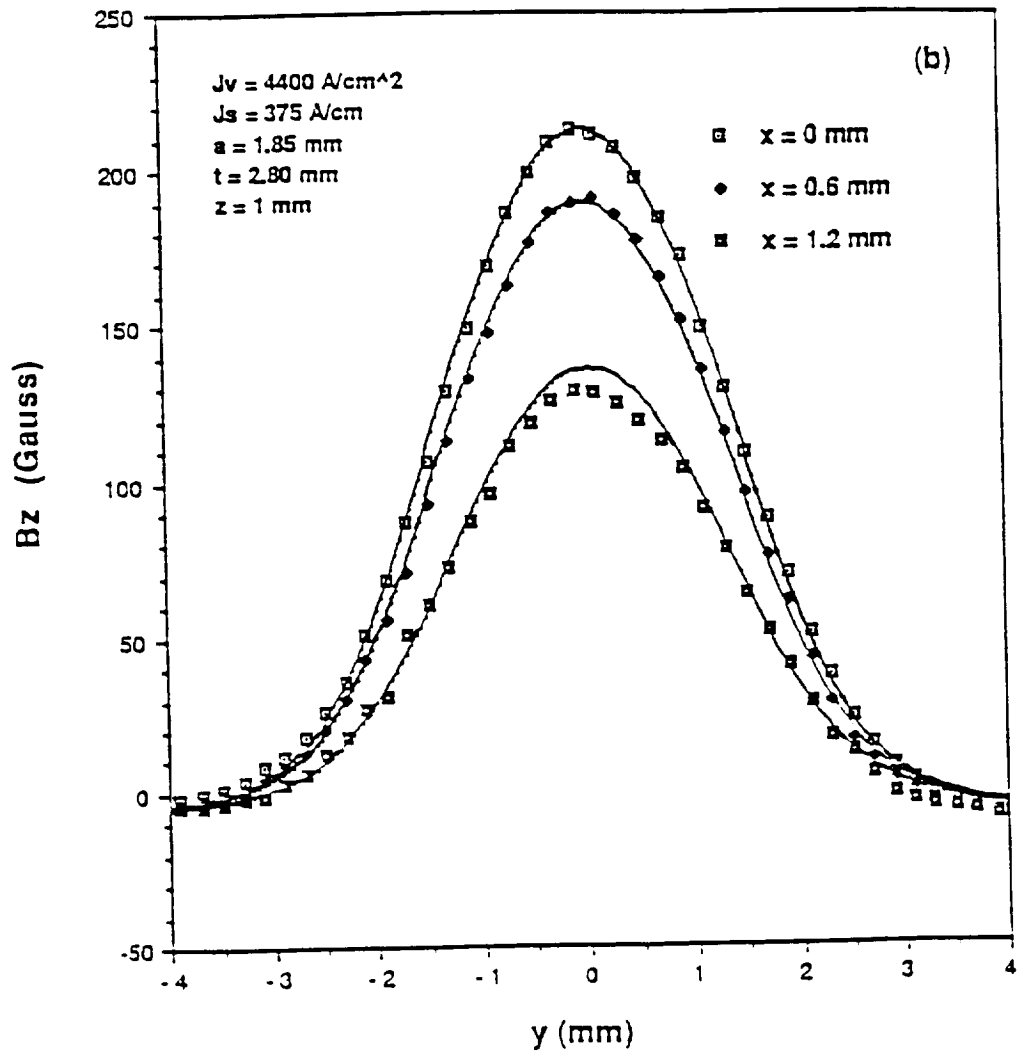


Fig. III.3 Fit of 2 Current Model to $B_t(x,y)$ for single grain of Y123 in a,b plane.

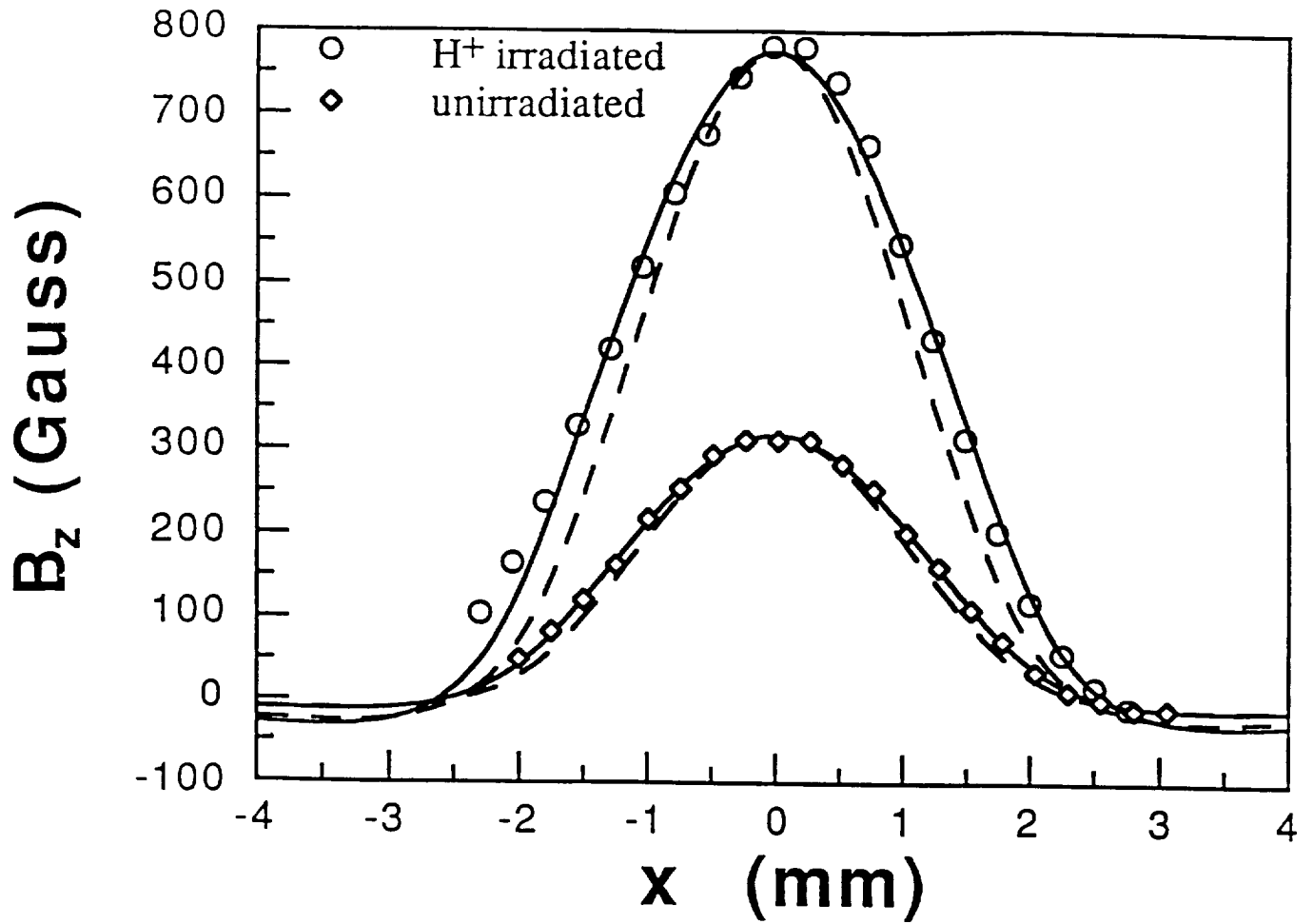


Fig. III.4 Fit of Two Current Model to B_t , for Y1+23 Tile. Measured field profiles are shown before and after irradiation with 200 MeV proton of a MT-Y123 disk sample with diameter $2a = 3.77$ mm, thickness $t = 1.4$ mm. Solid lines are fits of the $J_s + J_v$ theory, with $J_s = 265$ A/cm, $J_v = 9,450$ A/cm² for the unirradiated curve and $J_s = 1,115$ A/cm², $J_v = 18,950$ A/cm² for irradiated curve. In order to show the need for the J_s term, fittings are also shown for J_v only. Dashed lines are fittings with only $J_v = 11,700$ A/cm² for unirradiated and $J_v = 28,419$ A/cm² for irradiated cases, with $J_s = 0$.

superconductor, involves an increase of current in regions of low field. The rate at which J increases at low field is a parameter in the Kim-Bean model. In our work, low field is always at the outer surface of the sample. We believe that the J_s term, which we find is needed for melt-textured samples, simply represents the increase in J_c , in regions of low B , which characterizes the Kim-Bean model. This increased current is represented as a delta function at the surface in our model. We will site further evidence on this below.

We note, however, that our 2 component current mode is particularly useful because it is easier to fit to data than the Bean-Kim model in that *no iteration is required*. Thus, while the model may be an approximation to more complex physics, it is sufficiently accurate to fit the data for all cases we have encountered, and it is very easy to fit.

In the J_s+J_v model, the Z-component of the magnetic field $B_z(x,y,z)$, which is the usual quantity experimentally measured by a Hall probe, is given by

$$B_z(x, y, z) = \frac{J_s a}{c \sqrt{x^2 + y^2}} \int_0^{2\pi} d\varnothing' \cos \varnothing' \int_0^0 \frac{a^2 + (z - z')^2 - a \sqrt{x^2 + y^2} \cos \varnothing'}{-i \left[a^2 + x^2 + y^2 - 2a \sqrt{x^2 + y^2} \cos \varnothing' + (z - z')^2 \right]^{3/2}} dz' \\ + \frac{J_v}{c \sqrt{x^2 + y^2}} \int_0^{2\pi} d\varnothing' \cos \varnothing' \int_0^a r' dr' \int_0^0 \frac{r'^2 + (z - z')^2 - r' \sqrt{x^2 + y^2} \cos \varnothing'}{-i \left[r'^2 + x^2 + y^2 - 2r' \sqrt{x^2 + y^2} \cos \varnothing' + (z - z')^2 \right]^{3/2}} dz' \quad \text{Eq. III.1}$$

where z is the distance between the Hall probe and the sample surface, and a and t are the measured sample radius and thickness. Only J_s and J_v are adjusted to fit the data.

The model has successfully fit our measured $B_t(xyz)$ for sintered, melt textured, excess Y, $1H^+$, $3He^{++}$, and $4He^{++}$ and Uranium added materials. It has worked over 4 orders of magnitude in B_t , and 3 orders of magnitude in J_c .

C. Measurement of J_c

The currents J_s+J_v are both components of the critical current, J_c . There is more geometric detail in the J_s+J_v model than in a single number, such as is usually quoted for J_v . (This is also true in the Kim-Bean model, where a second parameter describes the variation of J_c vs. B). The J_s+J_v model describes the variation of J_c with position.

We may for the purposes of obtaining a single number for J_c , proceed as follows. Once one has fitted J_s and J_v to measured field points, the values of the currents may be used to compute the magnetic dipole moment, m . In terms of J_s and J_v , this is:

$$m = \frac{\pi a^2 t}{c} \left(\frac{1}{3} J_v a + J_s \right) \quad \text{Eq. III.2}$$

When J_c is "measured" on a Vibrating Sample Magnetometer (VSM), or SQUID, what is actually measured is m . On both VSM and SQUID, J_c is then *calculated* using some model of J_c , usually the Bean model⁽²³⁾.

We may do the same. Although m in Eq. III.2 is known to be composed of 2 components, we may ignore this, and calculate J_c using the Bean model.

Both the values of m and the subsequent values of J_c obtained by our method (field plots, plus fitting of the two current model) are experimentally found to agree to about 5 - 10 % with those found via VSM, or SQUID.

Fig. III.5, for example, shows measured field (discrete points) of the sample, both before and after proton irradiation. The J_s+J_v fittings to the two sets of data are shown as solid lines with the respective J_s and J_v values shown in the figure caption. The agreement between calculation using the model and measured data is again excellent, on both curves. Using the J_s and J_v values from the fits, the calculated values of m from Eq. III.2 are 1.34 emu and 3.60 emu before and after irradiation. The corresponding m values measured by VSM are 1.24 emu and 3.99 emu respectively at $B_A = 0$. Thus the J_s+J_v calculation and VSM measurement agree within 10%.

Note that the field-plot method for characterization of material, and measurement of J_c , is applicable to any successful current model, not only the Bean model, albeit with extra calculation.

D. A New Characterization Tool for J_c

There are several advantages to the field scan method, compared to VSM or SQUID measurements, for large industrial ingots of Y123.

First, VSM and SQUID are severely limited in the size of the sample which can be analyzed. On the other hand, the field plotting technique can be applied to any size sample. Thus the quality of large industrial batches can be quantified. Secondly, the field plot method dramatically exhibits any faults which may exist in the material. Fig. III.6 shows a sample with a weak link between 2 good regions. The "valley" of B_t in the weak link region, is readily seen. VSM or SQUID devices cannot detect such a valley except with repeated tests on bits of the product cut from the ingot. Used with a single sample, VSM or SQUID would give an average J_c , would have only randomly sampled small sections of the material, and could have entirely missed the faulty region.

Finally, the field plot method is dramatically cheaper than a VSM or SQUID. It would be surprising if its cost, as a commercial product, were not a factor of 5 lower than VSM or SQUID.

We have applied this technique in another way, in a collaborative effort with Salama's group in TCSUH, to evaluate the grain structure of a high T_c bus bar. Fig. III.7a shows results obtained on the microstructure of the polished bus bar, by Salama's group. Fig. III.7b shows the trapped field observed perpendicular to the large surface, by our group. The microstructure study shows a large grain in the region in which we find high field trapping. The dotted lines in that region in Fig. III.7a show the orientation of the a,b plane. The large grain at the left, which traps field well, has a c axis about 45° to the large surface. The large grain near the center, which does not trap high field, has a c axis almost perpendicular to the large surface. It is relatively clear, from this early result, that a *vector* plot of B_t would provide a very informative set of data on grain size and orientation. Thus the method described in this section may also serve some of the role of a photomicrograph, without the need to cut and polish the sample.

E. The Non Critical State

The above discussion applies to saturated magnetization (critical state), in which the trapped field has reached maximum value. We have recently extended the J_s+J_v model to

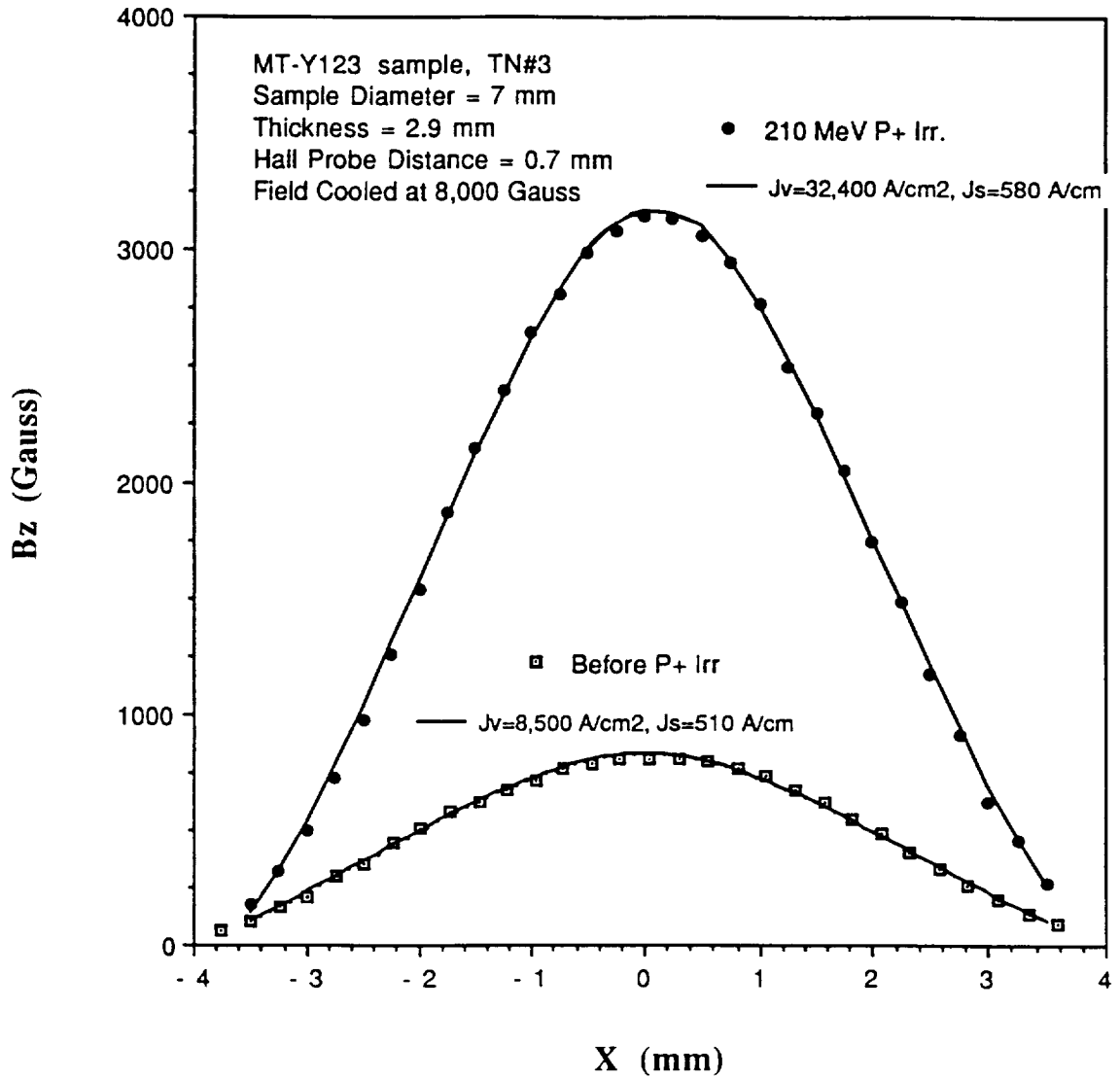


Fig. III.5 Fit of Two Current Model to B_t for MT Y1+23, Non-Irradiated and Irradiated.

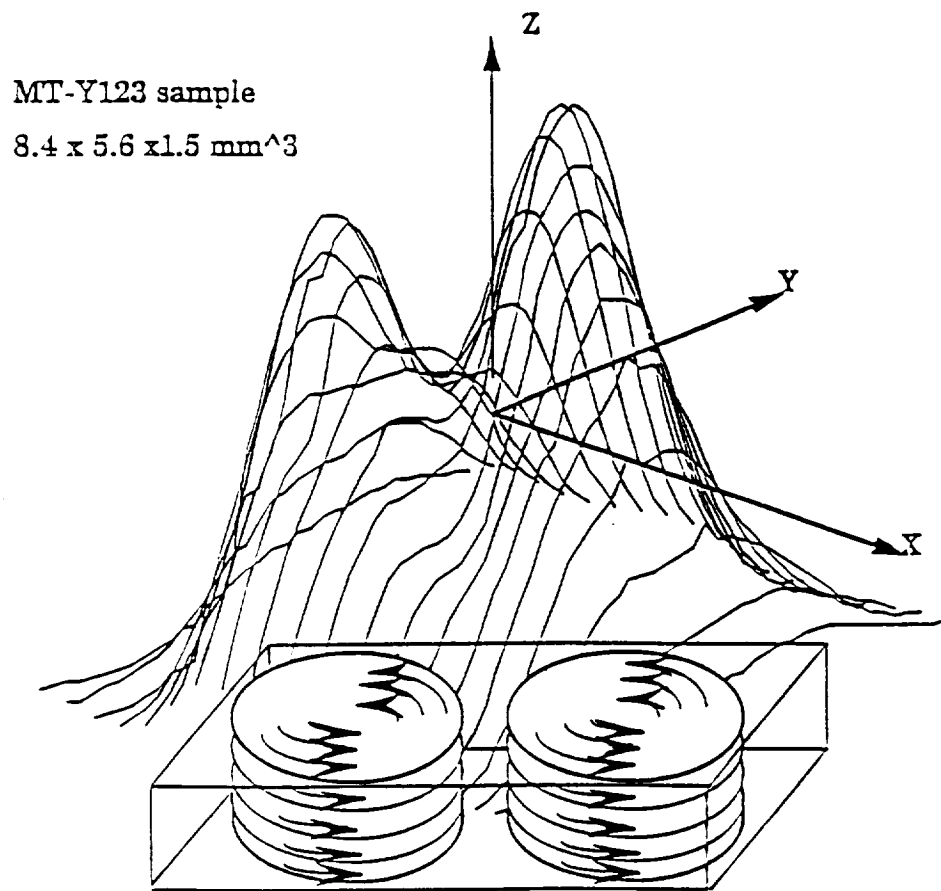


Fig. III.6 Field map of sample with a weak link between two good regions. Insert shows J_v current flow pattern.

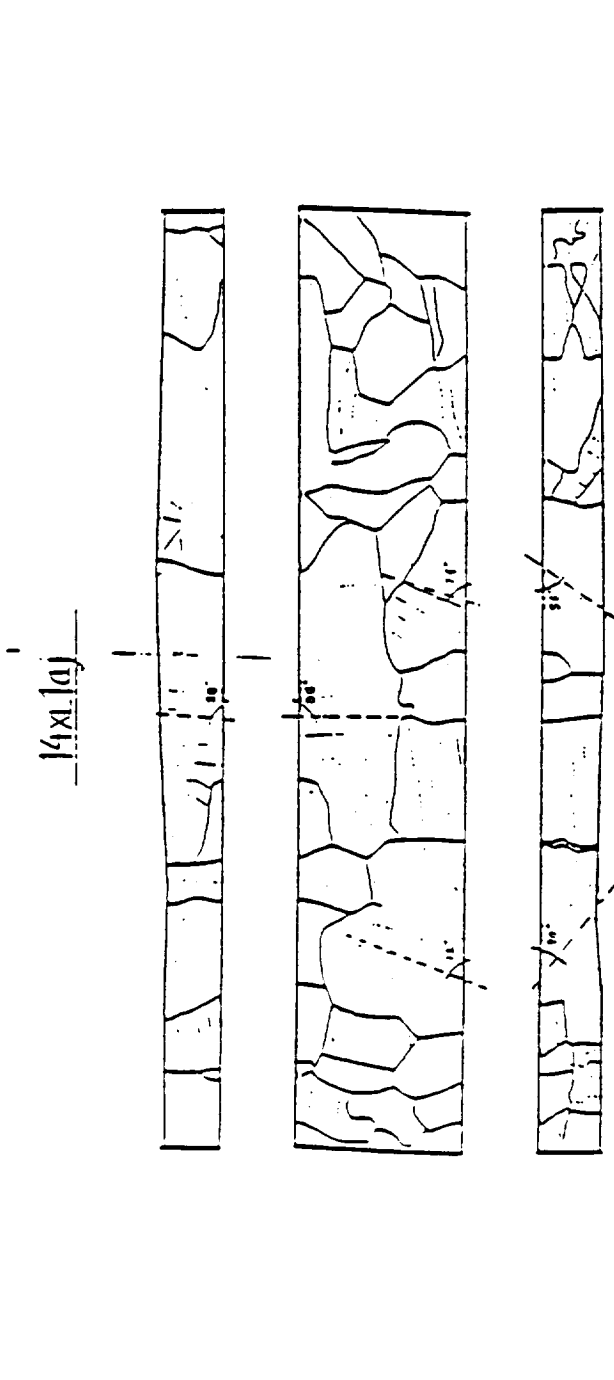


Fig. III.7a Photomicrograph of Salama bus bar.

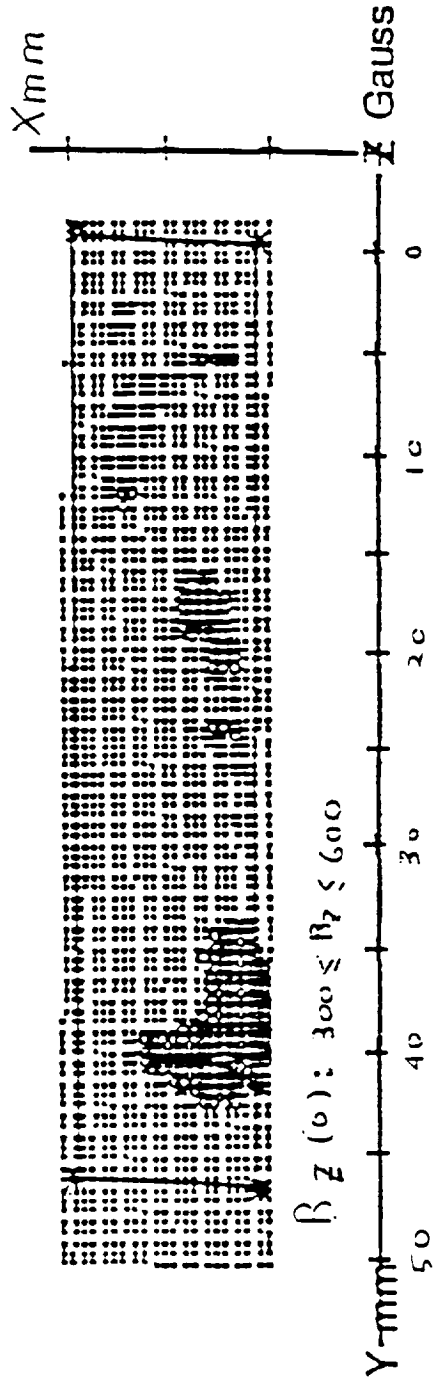


Fig. III.7b Field scan of same sample for B perpendicular to large surface.

Fig. III.7 Field Map of Grains in Bus Bar

situations in which the sample is not saturated, for both FC and ZFC procedures. According to the Bean model, the trapped field does not saturate in either FC or ZFC when the applied field $H < H^* (- (4\pi/c)J_c a)$. Fig. III.8a (top portion of the figure) shows the Bean field profiles under this condition for an infinitely long slab or cylinder in a parallel applied field. The FC case is shown in Fig. III.8a on the left, and ZFC is shown in Fig. III.8a, on the right. In each case the external field is on for the left and off for the right portions of the diagrams. After the external field is switched off, according to the Bean model, the supercurrent in a cylindrical superconductor flows in a *ring* in the FC case, and opposite currents flow in two rings of the same width in the ZFC case. The supercurrent patterns for our extended two-current model are shown in Fig. III.8b, with J_v bands similar to the Bean model. Unlike the Bean model, however, where the inner radii a_{in} and a_{mid} are determined only by J_c , a_{in} and a_{mid} in our J_s+J_v model are free parameters. Variable surface currents J_s and J_s' on the outermost and innermost radii of the sample are also included as adjustable parameters.

We stress here that the complication of a second adjustable parameter, such as J_s , is also required in a proper Bean model, as shown by Kim⁽²⁴⁾. In addition, our J_s+J_v model is simpler to use than any model such as Kim's with a field dependent $J_c = J_c(B)^{26,27}$.

Field profiles of an MT Y123 sample of diameter 7 mm and thickness 2.9 mm, with an applied field of 2 kG for both FC and ZFC, are shown in Fig. III.9. In the saturated state, the sample was determined to have $J_s = 550$ A/cm, and $J_v = 8,500$ A/cm² from field fitting, and magnetic moment $m = 17.2$ emu according to Eq. III.2. This leads to $J_c = 13,214$ A/cm² and $H^* = 5,812$ kG based on the Bean model. The solid lines in Fig. III.9 are best fits to the extended J_s+J_v model, with $J_v = 8,500$ A/cm², $J_s = 500$ A/cm², $J_s' = 0$, and a_{in} and a_{mid} values shown in the figure caption for FC and ZFC curves. Note that the same value of J_v results as in the saturated case. Also, note that the value of J_s is nearly the same as that required for a fit in the saturated case. The calculated curves based on the Bean model and the measured J_c are shown as dashed lines in Fig. III.9.

The a_{in} and a_{mid} values for the Bean model curves, determined by J_c as noted above, are grossly different from those in the J_s+J_v fits. For the ZFC case, in particular, the band widths for opposite J_c are of equal width in the Bean model, but the best J_s+J_v fit is obtained with unequal band widths for opposite J_v .

However, only B is amenable to direct measurement, not a_{in} and a_{mid} . We find the B field predicted by the Bean model is in *significant disagreement* with the measured field on both the FC and ZFC curves. See Fig. III.9. The B field predicted by the J_s+J_v model, on the other hand, is in very good agreement with the data. In the case of a saturated sample, discussed previously, the disagreement between the J_s+J_v model and the Bean model was very significant (See Fig. III.4), but not dramatic. In the unsaturated case the difference is dramatic. This is especially true in the ZFC case, where the Bean model is *off by a factor of 4*.

One may try to get better agreement for the Bean model by varying J_c . However, the Bean model curves do not change much with varying J_c . This is because the band width of the current density decreases as J_c increases, and vice versa, keeping the "total" current in the sample constant. Thus achieving a good fit to the data by varying J_c in the Bean model is impossible. The cause of the failure of the Bean model to fit the data is the field dependence of $J_c(B)$.

A two component current model such as Kim's, with $J_c = J_c(B)$, or ours, with J_s and J_v , is required. Either will do the job. The J_c model requires no iteration, such as required by Kim, and so is easier to use.

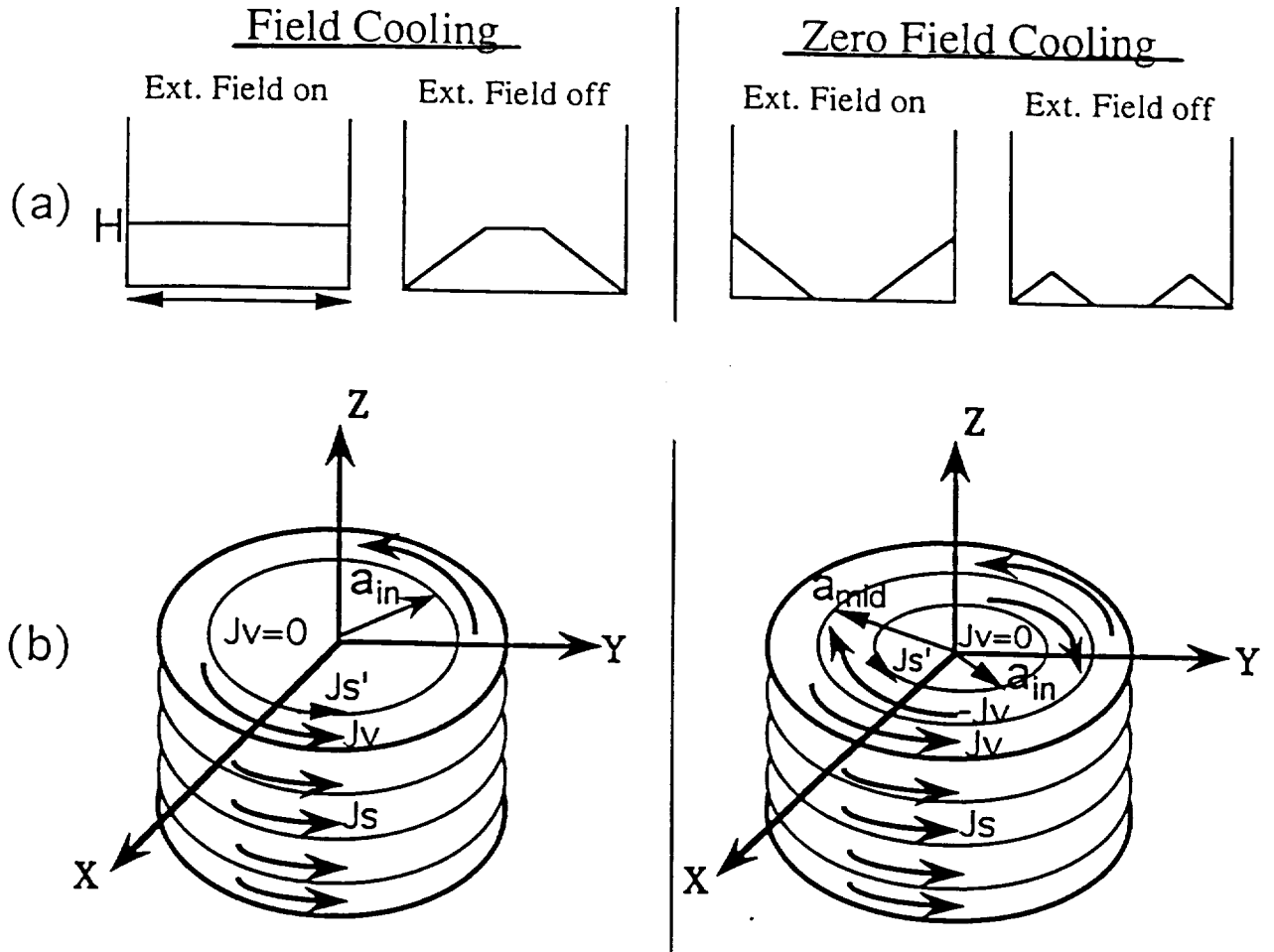


Fig. III.8 Schematics of current models in the unsaturated case. (a) Schematic field profiles based on the Bean model for an infinitely long slab or cylinder in a parallel applied field $H < H^*$, in both FC and ZFC procedures. (b) Current distributions inside a cylindrical superconductor in the extended $J_s + J_v$ model, when the sample is below saturation by both FC and ZFC.

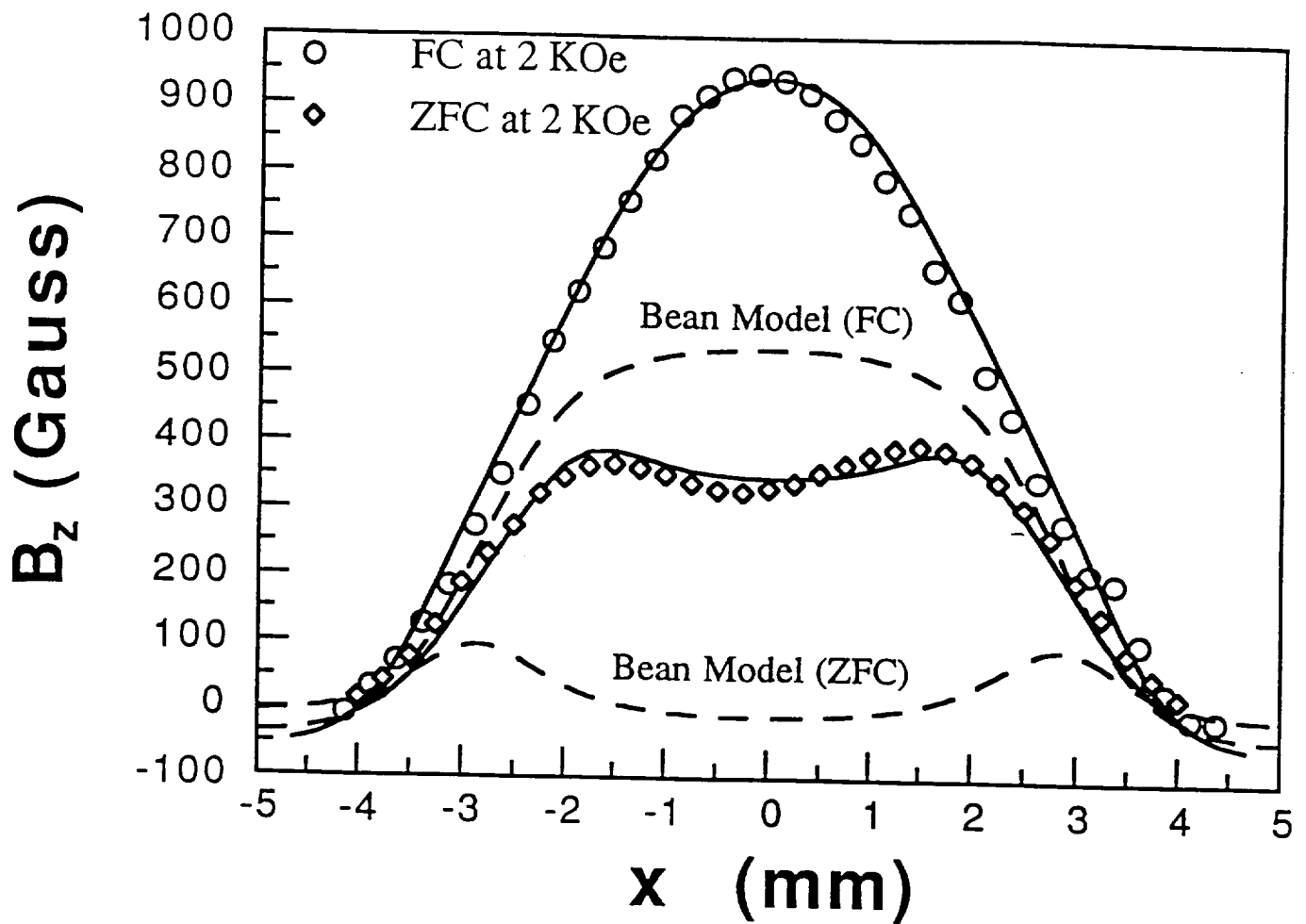


Fig. III.9 Field Map of MT Y1+23, In Unsaturated Case, showing FC and ZFC with an applied field of 2 kG. The sample is proton irradiated disk with 7 mm diameter and 2.9 mm thickness. Solid lines are fittings based on current distributions shown in Fig. III.8. For the FC curve, $J_s = 500$ A/cm, $J_v = 8,500$ A/cm², $J_s' = 0$, and $a_{in} = 0.9$ mm. For the ZFC curve, $J_s = 150$ A/cm, $J_v = 8,500$ A/cm², $J_s' = 0$, $a_{mid} = 1.91$ mm, and $a_{in} = 1.3$ mm. Dashed lines are fittings based on the Bean model with $J_c = 13,214$ A/cm², and $a_{in} = 2.3$ mm, $a_{mid} = 2.9$ mm determined from J_c and 2 kG applied field.

We noted earlier that J_s may play the role of a delta function representation of a Kim type rise in J_c in low field regions. We note that in the unsaturated case it is conceivable that there could be non-zero J_s at the both outer radius, a , and J_s' at the inner radius a_{in} . However, the best fits are obtained with a non-zero J_s , but with $J_s' = 0$. At the inner radius a_{in} , B_t is high, and one would expect the Kim type rise in J_c to be absent, while at the outer radius a , B_t is very low and the Kim type rise in J_c can be large. The finding that $J_s' = 0$ at the inner radius, for a best fit, provides an additional argument that J_s is the two component model representation of the Kim-type of behavior.

F. Conclusions Concerning Current Model

The two component J_s, J_v model fits all data taken by our group, to date. It is easier to apply than the broadly used Kim-Bean model, in the saturated (critical state) case.

The field plot method, without J_s, J_v interpretation, exhibits grain and weak link structure for arbitrarily large samples. Cost is low.

The combined field plot method and two component model provide a new, cheap method for J_c characterization applicable to arbitrarily large samples. Results of such characterization agree with broadly used VSM and SQUID measurements to 10%.

The two component (J_s, J_v) model fits the unsaturated case also, as does the Kim model. The Bean model fails severely in such a case.

We plan to continue studies of the J_s, J_v model to evaluate materials developed for shielding. Because the maximum field which can be shielded, $B_{s,max}$, is approximately equal to the field which can be trapped, $B_{t,max}$ fields of several Tesla can be shielded with these materials. It will be useful when doing tests to have an analytical model which can be easily applied. The J_s, J_v model will be extended to describe shielding, for this purpose.

IV. Creep

A. Creep Law, Critical State

In early measurements of B_t vs. time we noted a decrease in B_t with time (See Fig. IV.1). We determined that the data fit the general creep law

$$B_t(t_2) = B_t(t_1) [1 - \beta \log(t_2 - t_1)] \quad \text{Eq. IV.1}$$

where β is a constant⁽⁸⁾. (See Fig. IV.2) In this Section we will consistently use t in minutes.

The significant loss of trapped field was disconcerting, since our goal was permanent magnets. Note however, that due to the logarithmic nature of the law (Eq. IV.1), creep slows with time. The values of β observed⁽⁸⁾ were $\sim 4.3\%$ per decade of time (in minutes). Most of our observations commenced at $t = 10$ min. At $t = 10^4$ min (~ 1 week) B_t had decreased by $\sim 13\%$. However, due to the nature of Eq. IV.1, the decrease in B_t in the first week is equal to the decrease in B_t in the subsequent 19 years. Therefore creep did not kill the idea of HTS permanent magnets, but some "aging" would be needed if creep could not be slowed.

We have since tested Eq. IV.1 for sintered, melt textured, and excess Y variations of Y123, and found that Eq. IV.1 applies well in the interval $10 \text{ min} \leq T \leq 1 \text{ week}$, with $\beta = 0.043$, within 5%.

We have also tested creep in 1H^+ , 3He^{++} , and 4He^{++} irradiated materials. For these, creep appears to be 10-15% faster than for Y123 with naturally occurring pinning centers (See Fig. IV.3).

An observation of longer term creep indicates that there is a small but significant second order term to Eq. IV.1, which further *slows* creep at longer times. In an experiment lasting 6 weeks, creep slowed by the order of 20%. (See Fig. IV.4)

B. Creep, Non Critical State

In an early experiment we noted a dramatic decrease in creep when the sample was activated to $B_t < B_{t,\text{max}}$. See Fig. IV.5. We therefore performed creep tests on a variety of unsaturated samples (non critical state). In these cases we observed a decrease in β of Eq. IV.1.

$$\beta \propto (B_t/B_{t,\text{max}})^n \quad \text{Eq. IV.2}$$

where $n = 2 \pm 1$. An example of this is behavior shown in Fig. IV.6.

Thus, one can trade field magnitude for stability.

Much of the study of creep was done before we had a full understanding of the current model (Sec. III). Some critical observations will be repeated in the near future, to better ascertain the value of n in Eq. IV.2

Creep must also be tested for high Z columnar damage, and indeed for any new method of introducing pinning centers.

It will be particularly interesting, we believe, and amenable to basic analysis, to test creep as tailored pinning centers progress from the proton point defects, through the He^{++} , Li^{+++} "string of beads," to high Z columnar defects.

1000 Min + 88 Hour VIME Composit Graph

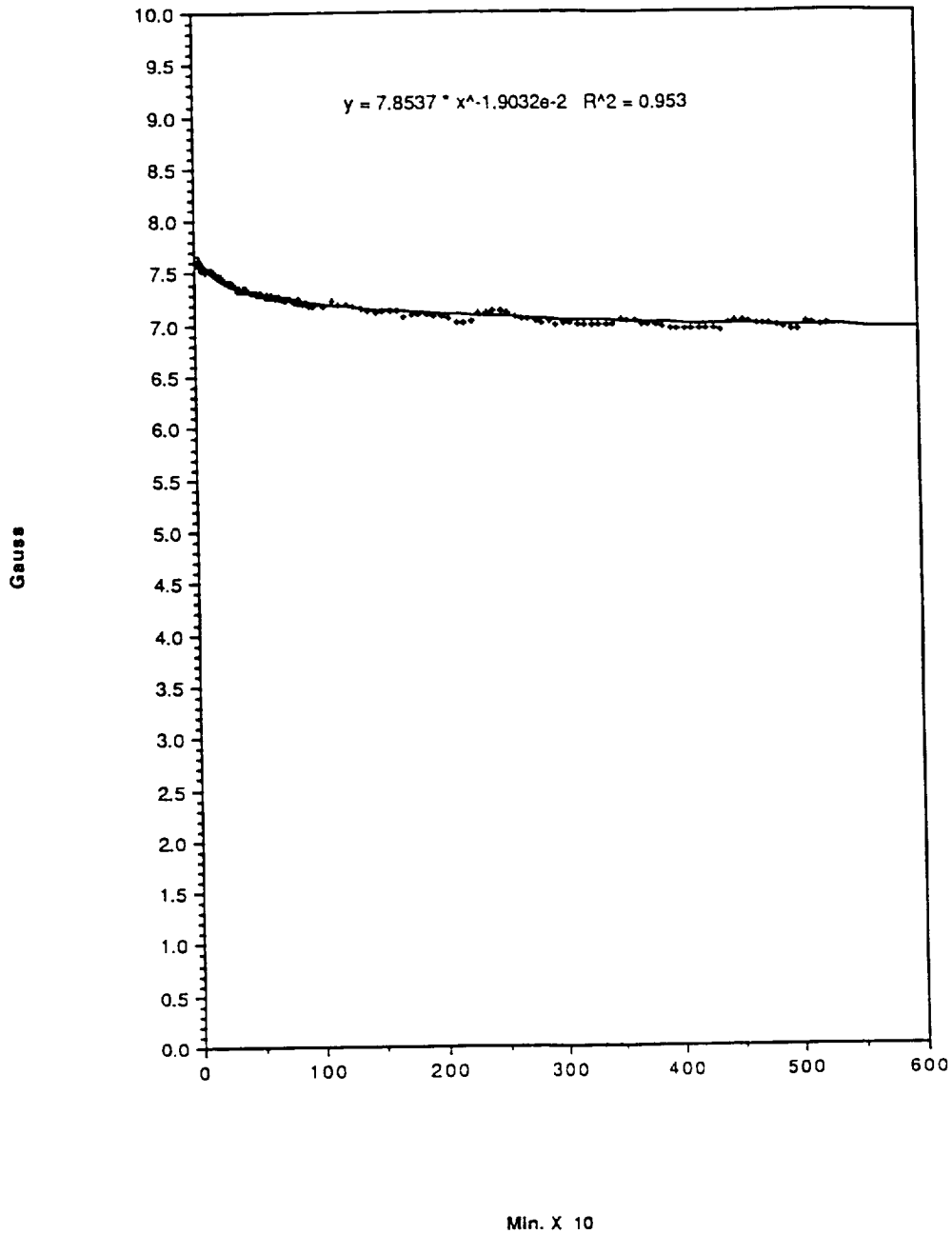


Fig. IV.1 Decrease of B_t , in HTS, vs. time. First creep observation by our group. Sintered sample of $d = 1.57$ cm is used. Solid line is power law fit $B_t = at^b$, $\beta = -0.019$.

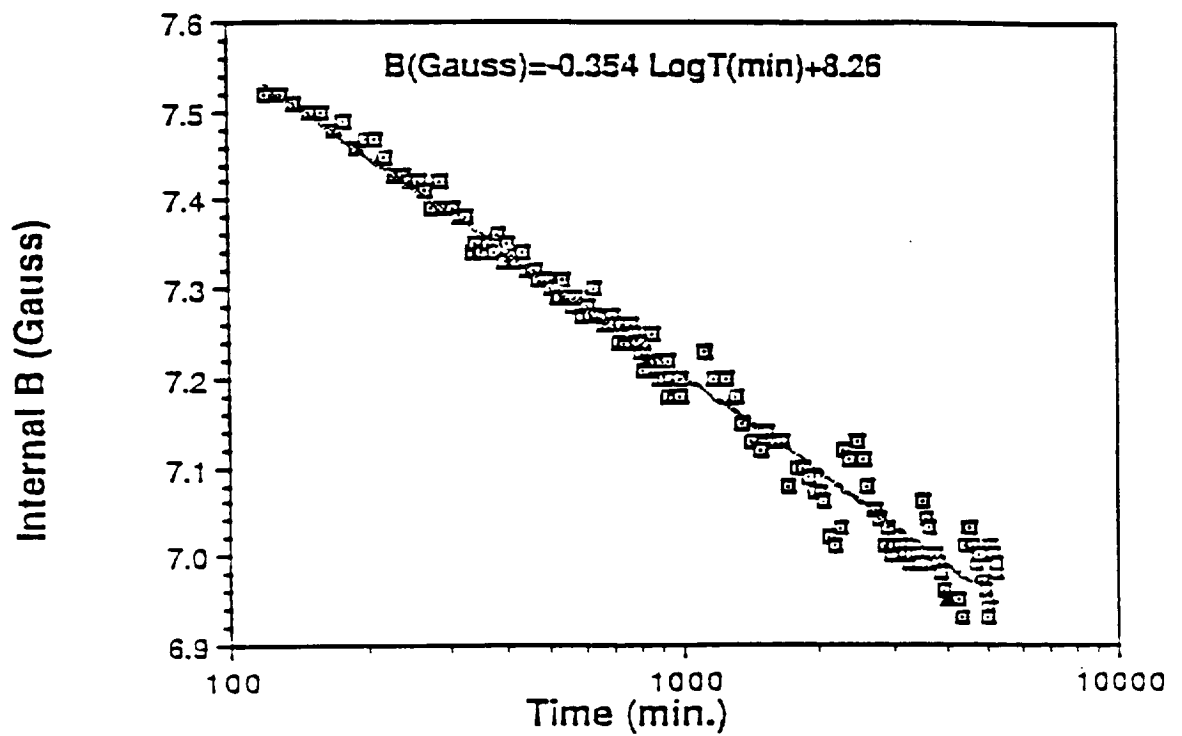


Fig. IV.2 Decrease of B_t in HTS vs. Log t . Creep measurement exhibiting logarithmic behavior of the form $B_t(t_2) = B_t(t_1)(1 - \beta \log[t_2 - t_1])$, with $\beta = 0.043$.

Data from "Data p.40 #3 & 85.1(Creep of #3"

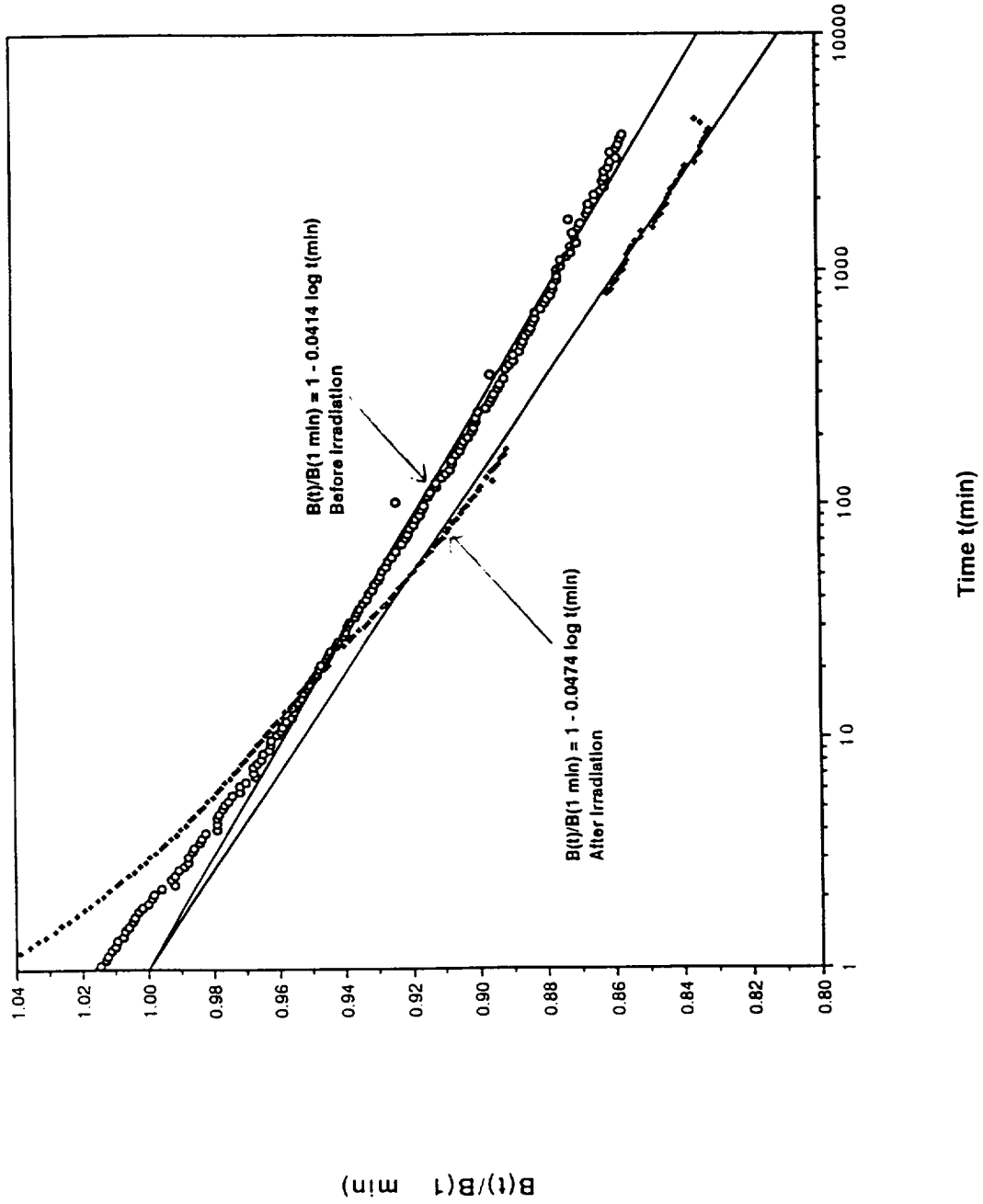


Fig. IV.3 Creep In unirradiated tile of MT Y1+23 vs. creep of same tile after proton irradiation. Data indicates a 12.6% increase in β as a result of irradiation by protons. He irradiation shows a smaller effect. Error in β is estimated = 5%.

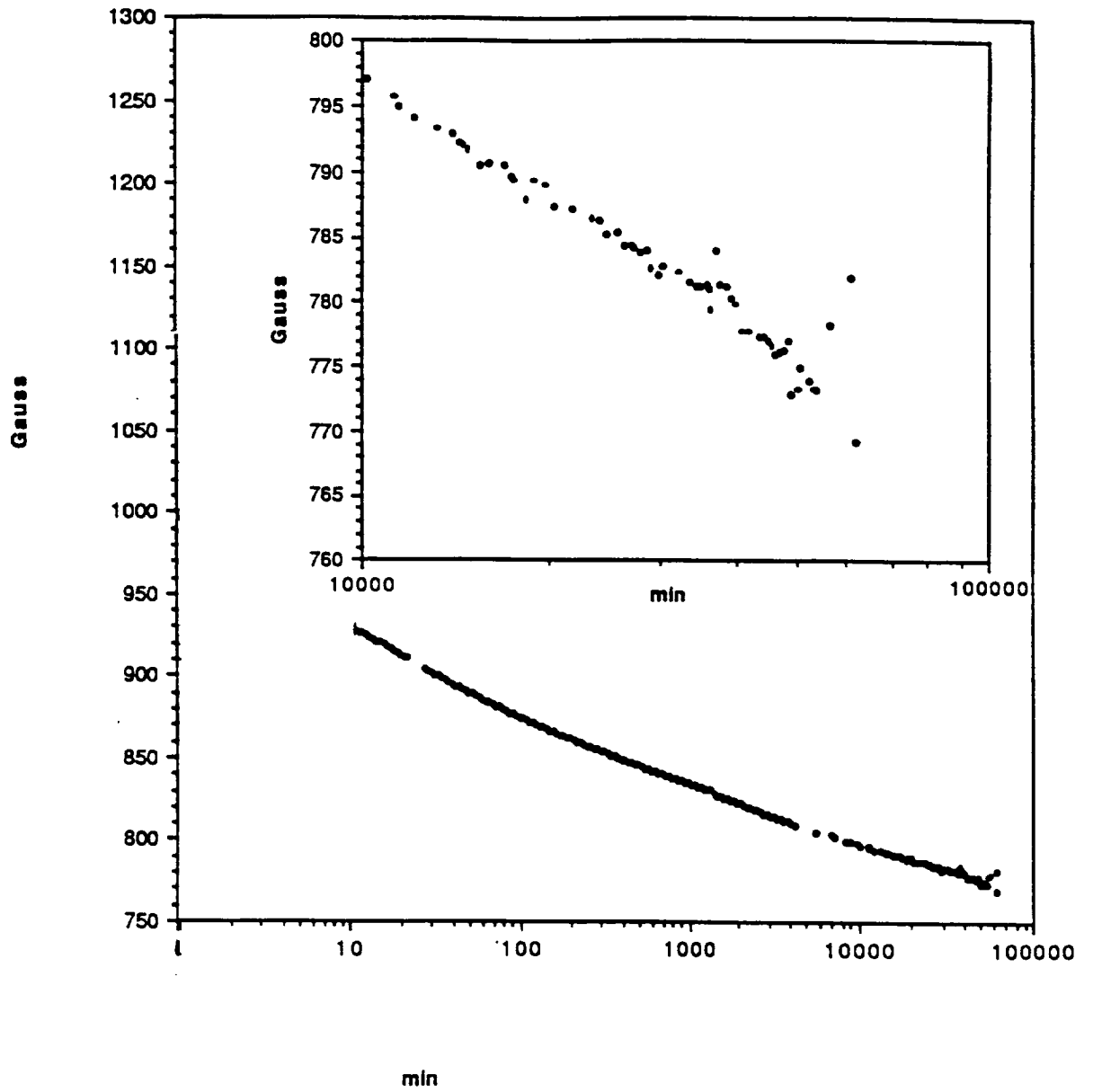


Fig. IV.4 Long term creep test (0.6×10^5 min). Note upward divergence of $B_t(t)$ from straight line approximation, reducing field loss at high t by about 30%.

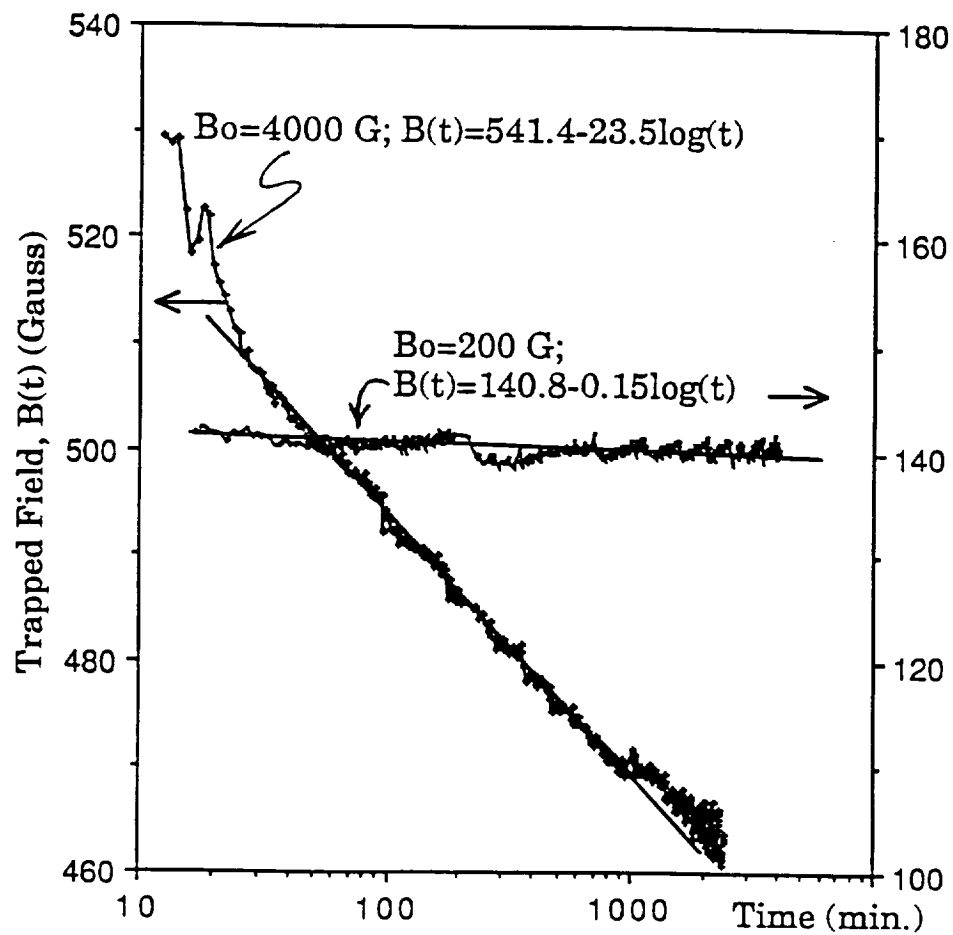


Fig. IV.5 Creep in saturated and unsaturated cases. Demonstration of the effect on creep of activating to $B_t < B_{t,max}$. Here β is reduced from 0.043 [at $B_t = B_{t,max} = 541$ G] to $\beta = 0.001$ at $B_t = 140$ G. ($\beta \sim [B_t/B_{t,max}]^{-2.6}$).

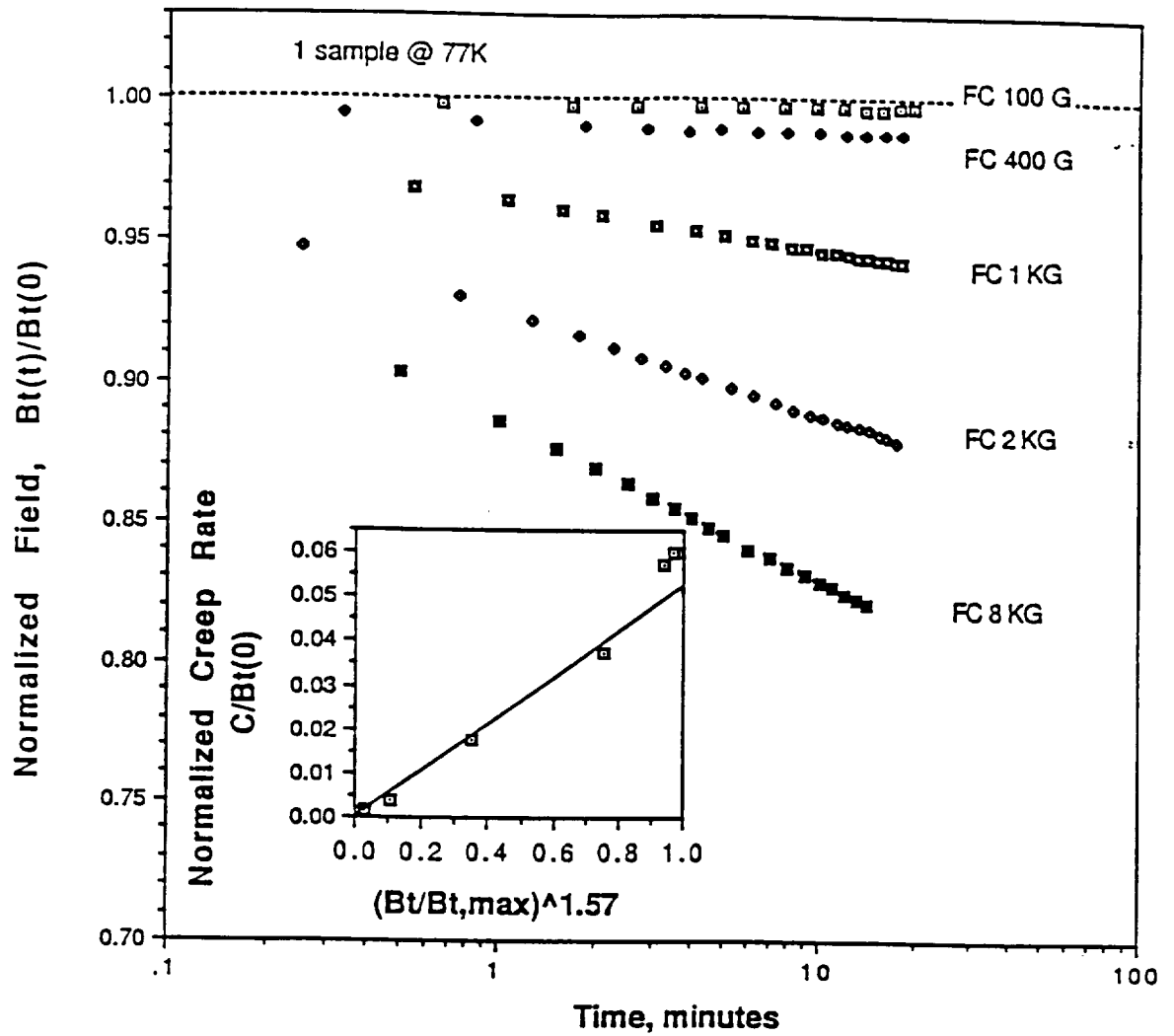


Fig. IV.6 Study of Creep as a function of $B_t/B_{t,max}$.

V. Prototyping

Early in our work we tried a Y123 magnet in a toy motor. A schematic of this experiment is shown in the top half of Fig. V.1. The magnet of the motor was excised, and the motor ran well with a Y211 replacement made up of four tiles ($B_t \sim 1\text{kG}$), until the bearings became frozen by the cold. The motor drew 3.5 watts of power. The intent of this experiment was (a) to make a first model, and (b) to see if the armature current affected the Y123 magnets.

A more serious prototype motor was run in collaboration with Emerson Electric Corp., Motor Div. (St. Louis) in Spring 1991. A schematic of the motor used is given in the lower part of Fig. V.1.

The motor had a three-phase stator in which a current of 0 to 8 Amps could be selected. The rotor had eight magnets mounted on eight steel bars. The bars were each one inch in diameter. The Emerson Electric team supplied the motor and controls. We supplied Y123 magnets. The space allowed for each of the eight magnets was one inch in diameter, and 0.2 inches thick. The stator used normal copper wire.

The motor ran well⁽²⁸⁾ and developed a torque of up to 80 oz. in. Power output of up to 19 Watts was obtained as the stator current was increased. The motor was run under various conditions for about three hours.

Fig. V.2 shows the data on torque vs. current in the armature. This plot should be a straight line unless (a) polarization of the iron pole faces by the armature current is providing a significant portion of the torque, or (b) there is a loss of magnetization of the Y123 with time. The data of Fig. V.2 are a reasonable fit to a straight line within the errors of the data points (square boxes).

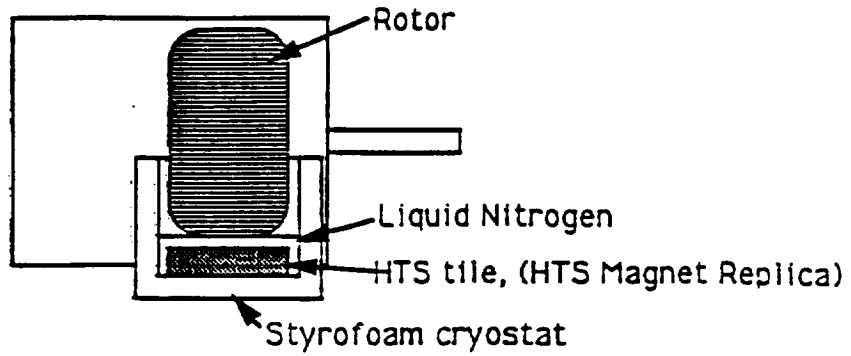
Emerson had contacted us through a third party. We were told that CPS Corp. had a DARPA contract under which they and Emerson were to produce a cold motor. Emerson was to produce the motor, and CPS was to deliver the high T_c trapped field magnets. However, we were told, CPS did not deliver the magnets. We met with Dick Crapo of Emerson at the DARPA/DOE Santa Fe meeting, in early 1991, to finalize our collaborative test. In the month that had elapsed since we were first contacted, CPS had delivered the magnets to Emerson. As a result, we had a chance to compare our high T_c magnets to those of CPS.

The Houston magnets were produced as a "side" effort, between February 7 and March 5, 1991, and were neither of large enough area to cover the Emerson pole faces, nor of sufficient thickness to fill the available gap. Nevertheless, the torque exerted by the Houston magnets was 2.6 times larger than that delivered by the full-size CPS magnets. Our method of fabrication, by assembly of laminations and mosaics, allows us to gain another factor of $2 \times 2.54 = 5.08$ by filling the pole area and gap, respectively. Houston magnets of the same volume as the CPS magnet should provide $2.5 \times 5.08 = 13.2$ times more torque than the CPS magnet.

The CPS point is also shown on Fig. V.2.

We have two additional collaborations in progress with Emerson. One is the operation of a generator using Y123 magnets. The second is a broader collaboration involving W.K. Chu of TCSUH at UH. In it, our group will design a motor using Y123 magnets in the rotor, and Cu wire in the armature - stator. We will also manufacture the rotor and produce the magnets. W.K. Chu will design and construct levitating bearings for the rotor, using our materials for levitation. Emerson will construct the Cu armature. We intend to measure efficiency in this prototype.

Hybrid-Electric Motor using High Tc SC Magnetic Replica
IBPD/TCSUH, 9/90



Emerson Electric Motors with HTS Magnet Replica
IBPD/TCSUH & Emerson Electric, 3/91

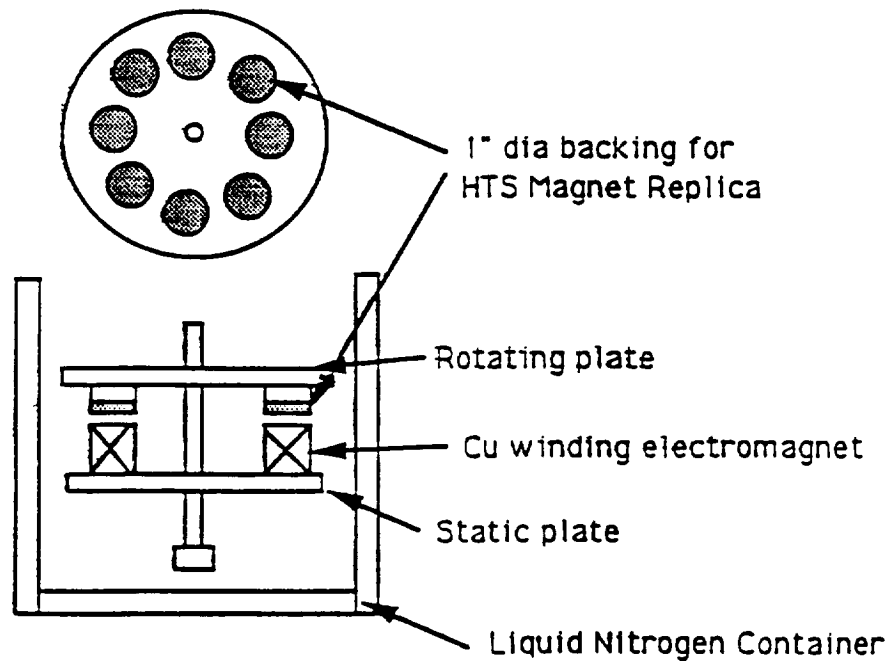


Fig. V.I. (Top) Toy motor prototype, and (bottom) Emerson Motor Prototype.

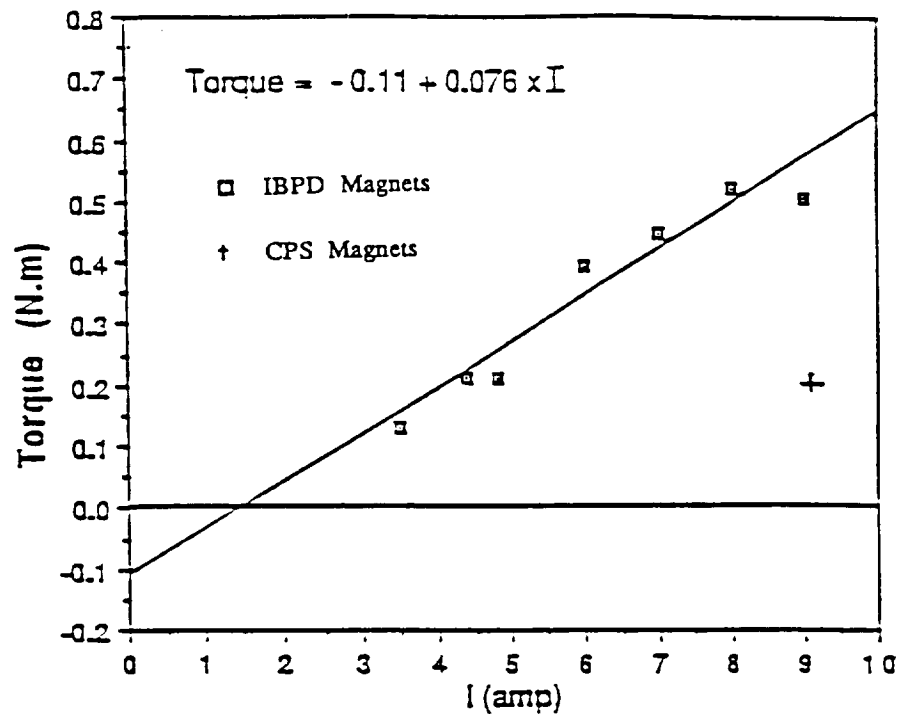


Fig. V.2 Torque vs. Current in Emerson Electric Co. Prototype Motor.

Beam Bending Magnet

We are also in the process of constructing a prototype of a very small bending magnet for charged particle beams, of the type used for external beam steering at accelerators. To date we have produced bending fields of 1 k Gauss, while exploring various geometries. Our ultimate goal is a uniform field of 15 k G, in a magnet composed of an iron yoke and Y123 magnets. We will however first construct a small version at 5 kG.

VI. References

1. M Rabinowitz, E. L. Garwin, and D. J. Frankel, *Lett. al Nuovo Cimento*, 7, 1 (1973)
2. M. Rabinowitz, *IEEE Magn.*, 11 (2), 548 (1975).
3. M. Rabinowitz, H. Arrowsmith, and S. Dahlgren, *Appl. Phys. Lett.*, 30 (11), 607 (1977).
4. C. W. Chu, et al, *Phys. Rev. Lett.*, 58, 405 (1988), and references therein.
5. J. T. Markert, et al., *MRS Bulletin*, Jan., 37 (1989); *Physics B*, 148, 155 (1987).
6. S. Jinn, et al., *Appl. Phys. Lett.*, 52, 2074 (1988).
7. K. Salama, et al., *Appl. Phys. Lett.*, 54, 2352 (1989).
8. R. Weinstein, et al., *Appl. Phys. Lett.*, 56, 1475 (1990).
9. R. Weinstein, I. G. Chen, J. Liu, and K. Lau, *J. Appl. Phys.*, 70, 6501 (1990).
10. R. Weinstein, I. G. Chen, J. Liu, *Proc. Symp. on R&D for the SSC*, Fort Worth, World Scientific Press (1990).
11. I. G. Chen and R. Weinstein, *Proc. of the TCSUH Workshop on HTS Bulk Materials*, Houston, World Scientific Press (1992).
12. M. Murakami, *ibid.*
13. M. Murakami, et al., *Japan Jour. of Appl. Phys.*, 28, 1189 (1989).
14. L. Civale, et al., *Phys. Rev. Lett.*, 67, 648 (1991).
15. R. Weinstein and I. G. Chen, *Proc. of the TCSUH Workshop on HTS Bulk Materials*, Houston, World Scientific Press (1992).
16. R. Weinstein, *Proc. World Congress on Superconductivity III*, Munich, Pergamon Press (1992).
17. R. L. Fleisher, et. al., *Phys. Rev. B*, 40, 2163 (1989).
18. Y. Ren, J. Liu, R. Weinstein, submitted to *Jour. Appl. Phys.* (Dec. 1992).
19. I. G. Chen, J. Liu, Y. Ren, R. Weinstein, submitted to *Appl. Phys. Lett.* (Dec. 1992).
20. H. Yamamoto, M. Chiba, T. Ogasawara, M. Tanaka, M. Morita and M. Hashimoto, *Proc. World Congress on Superconductivity III*, Munich, Pergamon Press (1992).
21. M. N. Wilson, *Superconducting Magnets*, Oxford Science Publications (1983).
22. I. G. Chen, J. Liu, R. Weinstein, and K. Lau, *Jour. Appl. Phys.*, 72, 1013, (1992).
23. C. P. Bean, *Phys. Rev. Lett.*, 8, 250 (1962); *Rev. Mod. Phys.*, 36, 31 (1964).
24. Y. B. Kim, C. F. Hempstead, and A. R. Strand, *Phys. Rev.*, 129, 528 (1963).
25. J. Liu, I. G. Chen, R. Weinstein, and J. Xu, *J. Appl. Phys.*, in press, (April 1993).
26. D. J. Frankel, *Jour. Appl. Phys.*, 50, 5402 (1979).
27. M. Daümling and D. C. Larbalestier, *Phys. Rev. B*, 40, 9350 (1989).
28. C. Gillespie, Editor, "One Small Step: An SC Motor is Tested Successfully," *Superconductor Industry*, Spring Issue 1993.

VII. Glossary of Terms

B_t	Magnitude of trapped magnetic field.
$B_{t,max}$	Maximum achievable trapped field for a given material, at a given temperature.
Creep	The gradual loss of field.
Critical State	J_c flows throughout sample.
FC	Method of activating a superconductor by cooling in an existing magnetic field.
Giant Flux Jump	Sudden loss of a significant portion of trapped field.
Grain	A crystal, but of poor quality. It may have intersecting planes at angles of typically $< 10^\circ$, voids, deposits of other chemicals.
HTS	High Temperature Superconductor
Light Ions	$1H^+$, $3He^{++}$, $4He^{++}$. In this work these are usually used at 200 MeV, to create pinning centers.
LTS	Low Temperature Superconductor
MT	Melt Textured
Non Critical State	$B_t < B_{t,max}$. J_c flows in only part of sample.
Pinning Center	A damage center, non superconducting region, or poorly superconducting region at which a flux quantum may be pinned.
Saturated State	See Critical State
SC	Superconductor
SQUID	Superconducting Quantum Interference Device
VSM	Vibrating Sample Magnetometer
Y123	$YBa_2Cu_3O_7$
Y1+23	Y123 with excess Y (usually 20 - 80%).
ZFC	Method of activating a superconductor by cooling at zero field, and then turning on the applied field.